


# Cleavage of VAMP2/3 Affects Oligodendrocyte Lineage Development in the Developing Mouse Spinal Cord

Christopher D. Fekete, Robert Z. Horning, Matan S. Doron, and  Akiko Nishiyama

Department of Physiology and Neurobiology, University of Connecticut, Storrs, Connecticut 06269

In the developing and adult CNS, new oligodendrocytes (OLs) are generated from a population of cells known as oligodendrocyte precursor cells (OPCs). As they begin to differentiate, OPCs undergo a series of highly regulated changes to morphology, gene expression, and membrane organization. This stage represents a critical bottleneck in oligodendroglialogenesis, and the regulatory program that guides it is still not fully understood. Here, we show that *in vivo* toxin-mediated cleavage of the vesicle associated SNARE proteins VAMP2/3 in the OL lineage of both male and female mice impairs the ability of early OLs to mature into functional, myelinating OLs. In the developing mouse spinal cord, many VAMP2/3-cleaved OLs appeared to stall in the premyelinating, early OL stage, resulting in an overall loss of both myelin density and OL number. The Src kinase Fyn, a key regulator of oligodendroglialogenesis and myelination, is highly expressed among premyelinating OLs, but its expression decreases as OLs mature. We found that OLs with cleaved VAMP2/3 in the spinal cord white matter showed significantly higher expression of Fyn compared with neighboring control cells, potentially because of an extended premyelinating stage. Overall, our results show that functional VAMP2/3 in OL lineage cells is essential for proper myelin formation and plays a major role in controlling the maturation and terminal differentiation of premyelinating OLs.

**Key words:** Fyn; myelin; oligodendrocyte precursor; SNARE; spinal cord; VAMP

## Significance Statement

The production of mature oligodendrocytes (OLs) is essential for CNS myelination during development, myelin remodeling in adulthood, and remyelination following injury or in demyelinating disease. Before myelin sheath formation, newly formed OLs undergo a series of highly regulated changes during a stage of their development known as the premyelinating, or early OL stage. This stage acts as a critical checkpoint in OL development, and much is still unknown about the dynamic regulatory processes involved. In this study, we show that VAMP2/3, SNARE proteins involved in vesicular trafficking and secretion play an essential role in regulating premyelinating OL development and are required for healthy myelination in the developing mouse spinal cord.

## Introduction

During development, the generation of new oligodendrocytes (OLs) is essential for proper CNS myelination. Once established, mature OLs appear to be exceptionally stable and long lived, persisting well into adulthood (Tripathi et al., 2017) and for

decades in the human brain (Yeung et al., 2014). Despite the apparent stability of established OLs, oligodendroglialogenesis continues throughout adulthood, contributing to experience-dependent myelination and remodeling (Young et al., 2013; Hughes et al., 2018).

Both during development and in adulthood, OLs are derived from oligodendrocyte precursor cells (OPCs), a population of proliferative cells that persists throughout adult life (Kessaris et al., 2006; Nishiyama et al., 2016). During differentiation, OPCs must undergo a series of progressive changes in morphology, cell to cell interactions, and gene expression to achieve the specialized structure and function of mature, myelinating OLs. These steps are highly regulated and a significant portion of newly formed OLs fail to integrate and are lost (Barres et al., 1992; Trapp et al., 1997; Hughes et al., 2018; Sun et al., 2018). This stage of OL development is often referred to as the early OL or premyelinating OL stage and typically lasts for 2–3 d in mice (Hill et al., 2014; Hughes et al., 2018). In zebrafish, the formation of new myelin sheaths has been shown to occur over just a 5-h

Received Nov. 3, 2021; revised Oct. 20, 2022; accepted Aug. 15, 2023.

Author contributions: C.D.F., R.Z.H., and A.N. designed research; C.D.F., R.Z.H., M.S.D., and A.N. performed research; C.D.F., R.Z.H., M.S.D., and A.N. analyzed data; C.D.F. wrote the first draft of the paper; C.D.F., R.Z.H., M.S.D., and A.N. edited the paper.

This work was supported by National Institutes of Health (NIH) Grants R01NS116182 and R01NS073425 and National Multiple Sclerosis Society Grants PP-1809-32554 and RG-1612-26501 (to A.N.). The Leica SP8 confocal was purchased using funds from the NIH Instrumentation Grant S10 OD016435 (to A.N.). We thank Youfen Sun for maintaining transgenic mouse lines, Dr. Chris O'Connell for assistance with confocal microscopy, and Jessica Ulbrich and Owen Greene for assistance with immunofluorescence labeling. We also thank Dr. Brad Zuchero and Dr. Mable Lam (Stanford) and Dr. Ye Zhang and Dr. Lin Pan (University of California, Los Angeles) for many helpful discussions.

The authors declare no competing financial interests.

Correspondence should be addressed to Akiko Nishiyama at akiko.nishiyama@uconn.edu.

<https://doi.org/10.1523/JNEUROSCI.2206-21.2023>

Copyright © 2023 the authors

period, further highlighting the need for strict temporal control over this process (Czopka et al., 2013).

One of the signaling molecules known to play an important role in regulating this process is the Src kinase Fyn, which is thought to be an important component of the axon-OL signaling axis required to initiate myelination (Umemori et al., 1994; Laursen et al., 2009; White and Krämer-Albers, 2014). Fyn has been shown to regulate early OL survival, morphology, and the timing of major myelin-associated gene expression (Colognato et al., 2004; White et al., 2008; Mitew et al., 2014; Matrone et al., 2020). Recent work has even shown that modulating Fyn activity during a critical time window of new myelin sheath formation can alter the number of myelin sheaths a given cell will form (Czopka et al., 2013).

Like all eukaryotic cells, OL lineage cells employ SNARE-mediated membrane fusion to enable secretion, vesicle and membrane trafficking, as well as targeting and sorting of membrane proteins, crucial functions in OL development (Feldmann et al., 2009; Fekete and Nishiyama, 2022). In the OL lineage, inhibition of vesicle-associated SNARE proteins VAMP3 or VAMP7 was shown to impair the trafficking and surface presentation of myelin proteolipid protein (PLP) in the OPC cell line, Oli-neu, and primary oligodendrocyte cultures (Feldmann et al., 2011). The transcription of myelin basic protein (MBP) has also been shown to be regulated by syntaxin 4, a target-membrane associated SNARE protein (Bijlard et al., 2015).

In order to better understand the role that SNARE mediated processes play in early OL lineage development, we used the iBot mouse line which expresses the light chain of Botulinum toxin type B (BoNT/B-LC) in a cre-dependent manner (Slezak et al., 2012; Lam et al., 2022; Pan et al., 2023). BoNT/B is a potent neurotoxin which blocks SNARE-mediated processes by cleaving VAMP1–VAMP3 (G.G. Schiavo et al., 1992; Humeau et al., 2000; Chen et al., 2008; Yamamoto et al., 2012). The light chain of BoNT/B contains the catalytically active portion of the toxin but lacks the heavy chain required for the toxin to enter into cells, restricting the toxin's access to a targeted population of cells.

Here, we crossed iBot mice with NG2cre mice to impair VAMP1–VAMP3-mediated exocytosis in OPCs and their progeny. OL lineage cells primarily express VAMP2–VAMP4 and VAMP7 (Feldmann et al., 2009; Zhang et al., 2014); however, since VAMP4 and VAMP7 are not targeted by BoNT/B, we primarily inhibited VAMP2/3-dependent processes. We found that cleavage of VAMP2/3 in this population resulted in spinal cord hypomyelination and a reduction in the number of mature OLs formed. Interestingly, we did not detect major changes in OPC generation, proliferation, or their terminal differentiation into OLs. Based on our results, VAMP2/3 function becomes critical during the final development of early OLs into mature OLs, as cleavage of VAMP2/3 impaired their ability to fully mature into stably integrated, myelinating OLs.

## Materials and Methods

### Animals and transgenic mouse lines

All animal procedures received approval by the Institutional Animal Care and Use Committee at the University of Connecticut. To cleave VAMP1–VAMP3 in oligodendrocyte lineage we crossed heterozygous iBot mice (iBot<sup>tg/+</sup>) with homozygous NG2cre mice (NG2cre<sup>tg/tg</sup>). Here, we will refer to iBot<sup>tg/+</sup>NG2cre<sup>tg/+</sup> animals as iBot<sup>tg/+</sup> mice and control iBot<sup>+/+</sup>NG2cre<sup>tg/+</sup> animals as iBot<sup>+/+</sup> mice. The iBot mice express cre-dependent BoNT/B-LC followed by an IRES and EGFP reporter (The Jackson Laboratory; stock #018056; B6.FVB-Tg(CAG-boNT/B,EGFP)

**Table 1. Primer sequences**

Gene	Forward primer (5' to 3')	Reverse primer (5' to 3')	Usage
Mouse iBot	cgtgttccactcgaagagt	ggcaaaacttcattgctt	Genotyping
Mouse Cre	ccgtacaccaaaattgcc	atcgcgaacattccagg	Genotyping
Mouse <i>Mbp</i>	acacagagaactaccattatgg	tggttcgaggtgcacaatgttctt	qPCR
Mouse <i>Cnp1</i>	ctctactttggctgttctgac	gcttctctgggttcatctcc	qPCR
Mouse <i>Plp1</i>	cctagcaagacctgtccagta	ggacagaaggttgagccaca	qPCR
Mouse <i>Myrf</i>	gtgtcatcgcccaggaagtga	cattctcatgaagattcgctc	qPCR
Mouse <i>Rn7sk</i>	Ctccaaacaagctcgaagtgcca	atgcagcgcctcattggtatgt	qPCR

U75-56Fwp/J; Slezak et al., 2012). The NG2cre mice used were originally generated using a BAC construct containing NG2creER but were found to express cre in NG2+ cells independent of tamoxifen induction (Zhu et al., 2011). Both male and female offspring postnatal day (P)13–P14 were used for all experiments. iBot<sup>tg/+</sup> mice were identified either by genotyping PCR or on the basis of their motor function with subsequent confirmation of GFP expression. Primer sequences used for genotyping can be found in Table 1. For EdU pulse chase experiments, animals were injected with 50 mg/kg EdU (Cayman, 20518) three times with 2 h between injections at P10 before being killed at P13.

### Dissociated cultures of rat OPCs and *Vamp2/3* knock-down

Mixed glial cultures were prepared from the spinal cords of P1–P4 Sprague Dawley rats (Charles River Laboratories) and maintained in DMEM supplemented with 10% fetal calf serum (Invitrogen) as previously described (Nishiyama et al., 2010; Dugas and Emery, 2013; Medved et al., 2021). To obtain cultures enriched for OPCs, loosely adherent cells, most of which were OPCs, were dislodged from the surface of mixed glial cultures by pipetting, preplated on uncoated tissue culture dishes to remove microglia and astrocytes, and plated on glass coverslips coated with 100 μg/ml poly-L-lysine at a density of 50,000–100,000 cells/12-mm coverslip. The cells were grown for 1 d in serum-free growth medium containing 50 ng/ml platelet-derived growth factor (PDGF) AA (Peprotech, #315-17) and 5 ng/ml neurotrophin-3 (Peprotech, #450-03). They were then transduced with lentiviral vector (MOI of 2) containing control GFP (OriGene Technologies, TR30021V), *Vamp2*shRNA-GFP (OriGene TL709295VA), or *Vamp3*shRNA-GFP (OriGene TL712338VB). After 1 d in growth medium, the cells were switched to differentiation medium containing Sato's medium supplemented with ciliary neurotrophic factor (Peprotech 450-50), 400 ng/ml triiodothyronine (Sigma-Aldrich, T6397), and 10 μg/ml forskolin (Sigma-Aldrich, F6886). After 6 d in differentiation medium, with medium change every 2–3 d, the cells were fixed in 4% paraformaldehyde for 15 min at room temperature (RT), blocked and permeabilized at RT for 30 min, incubated in mouse anti-MBP antibody (Smi99, BioLegend, 8808401) for 30 min at RT, and washed and incubated in Cy3-conjugated goat anti-mouse IgG2b (Jackson ImmunoResearch 115-165-207) for 30 min. Following washes, the coverslips were mounted on glass slides using Vectashield with DAPI (Vector Laboratories, H-1200).

### qRT-PCR

For relative RNA quantification, total RNA from the spinal cords of three P13 iBot<sup>tg/+</sup> and three P13 iBot<sup>+/+</sup> mice were isolated using PureLink RNA Mini kit (Invitrogen), and DNA was removed by DNase I digestion. After the integrity of the extracted RNA was confirmed with an Agilent 4200 High Sensitivity RNA Screen Tape Assay (Center for Genome Innovation, University of Connecticut), 2 μg of total RNA from each sample was reverse transcribed using Superscript IV (Invitrogen) and a mixture of 20 μM random hexamer and 20 μM oligo(dT)<sub>20</sub> primers. Subsequent qPCR was conducted on a CFX06 Real-Time PCR Detection System (Bio-Rad) using the primers listed in Table 1 at 300 nM (Integrated DNA Technologies) and SYBR Green (Invitrogen).

### SDS-PAGE and Western blot analysis

For immunoblotting, spinal cords from P14 iBot<sup>tg/+</sup> and iBot<sup>+/+</sup> mice were either processed immediately or snap-frozen in liquid nitrogen and stored at –70°C until further processing. Protein was extracted via homogenization with a Dounce or plastic pestle homogenizer in 150–

**Table 2. Source and dilutions of antibodies used**

Antibody	Dilution	Source	Catalog #	RRID
Ms a-ALDH1L1, clone N103/39	1:100	Biologend	856802	AB_2783464
Ms a-APC, clone CC1	1:500	Calbiochem	OP80	AB_2057371
Rb a-ASPA	1:500	Millipore	ABN1698	AB_2827931
Rb a-cleaved caspase 3 (Asp175)	1:400	Cell Signaling	9664	AB_2070042
Ms a-CNPase, clone SMI-91	1:500	Millipore	NE1020	AB_2043400
Rb a-Fyn	IF-1:200 WB-1:1000	Cell Signaling	4023	AB_10698604
Ms a-GAPDH, clone 6C5	1:2000	Millipore	MAB374	AB_2107445
Ck a-GFP	1:1000	Aves Labs	GFP-1020	AB_10000240
Rb a-GST $\pi$	1:500	MBL International	312	AB_591792
Gt a-Iba1	1:500	Invitrogen	PA5-18039	AB_10982846
Ms a-MBP, clone Smi99	1:2000	Biologend	808403	AB_2734562
Rb a-MBP	1:2000	Chemicon	AB980	AB_11211843
Ms a-NKX2.2	1:150	DSHB	74.5A5 <sup>1</sup>	AB_531794
Ms a-Olig2, clone 211F1.1	1:1000	Millipore	MABN50	AB_10807410
Gt a-PDGFR $\alpha$	1:500	R&D Systems	AF1062	AB_2236897
Rt a-PLP/DM20, clone AA3	1:2	Gift from Dr. Kaz Ikenaka, Okazaki, Japan		
Ms a-PLP, clone PLPC1	1:1000	Millipore	MAB388	AB_177623
Ms a-QK17, clone N183/15	1:1000	NeuroMab	75-200	AB_2173148
Rb a-pY416 Src family kinase	1:500	Cell Signaling	6943	AB_10013641
Rb a-VAMP3	1:1000	Novus	NB300-510	AB_2304177

74.5A5 was deposited to the DSHB by Jessell, T.M./Brenner-Morton, S.

300  $\mu$ l RIPA buffer containing 1 $\times$  Halt Protease inhibitor cocktail (ThermoFisher) and 1 $\times$  PhosSTOP (Roche or Sigma; VAMP3 and FYN Western blot analyses only), after which the homogenates were incubated on ice for 10–30 min. The lysate was then cleared by centrifugation at 13,000  $\times$  g for 10–15 min at 4°C. Protein concentration was measured using the DC Protein Assay kit (Bio-Rad), a detergent compatible modification of the Lowry method. Cleared lysates were heated for 10 min at 70°C in reducing sample buffer. For each sample, 50–100  $\mu$ g of protein in 10–40  $\mu$ l volume was electrophoresed through 8% or 12% Bolt Bis-Tris Plus gels (Invitrogen) in Bolt MOPS or MES SDS running buffer (ThermoFisher) and transferred to Immobilon-FL membrane (Millipore) in a transfer buffer consisting of 1.25 mM Bicine, 1.25 mM Bis-Tris, and 1 mM EDTA (pH 7.2) at 100 V for 1–1.5 h in a chilled blotting cell. The membranes were blocked for 1 h at room temperature in Odyssey PBS or TBS blocking buffer (LI-COR) and then incubated in primary antibodies (Table 2) diluted in blocking buffer containing 0.1% Tween 20 overnight at 4°C. Following four washes in PBS or TBS containing 0.1% Tween 20, the membranes were incubated in secondary antibodies conjugated with IRDye680 or IRDye800 (LI-COR) diluted in blocking buffer containing 0.1% Tween 20 and 0.01% SDS for 1 h at room temperature. After four washes in PBS or TBS with 0.1% Tween 20, the membranes were imaged on an Odyssey Infrared Imaging System (LI-COR) using Odyssey Imaging Software (LI-COR). The intensity of the bands was quantified using Image Studio Lite Quantification Software (LI-COR) or using the FIJI distribution of ImageJ (Schindelin et al., 2012).

#### Tissue processing and immunofluorescent labeling

To prepare the spinal cords used in this study, mice were perfused first with a PBS rinse followed by 4% paraformaldehyde with 0.1 M L-lysine and 0.01 M sodium metaperiodate in 0.1 M phosphate buffer (PB). The tissue was then harvested and postfixed for 1–3 h in the same fixative at 4°C before being washed four times in 0.2 M PB, leaving the tissue overnight in the fourth wash at 4°C. The tissue was then moved to 30% sucrose in 0.1 M PB for cryoprotection. After cryoprotection, the tissue was embedded in frozen O.C.T. compound (Sakura Tissue Tek or Fisher brand O.C.T.); 20  $\mu$ m sections were cut onto Superfrost Plus slides (Fisherbrand) using a Leica CM3050S cryostat, and 40- $\mu$ m free floating sections were cut using a freezing microtome.

For immunofluorescent labeling, sections were washed three times in 10 mM PBS and blocked with 5% normal serum (either donkey or goat) and 0.3% Triton X-100 in PBS. An additional 5% BSA was included when blocking before using bovine-raised secondary antibodies. After

blocking, tissue sections were incubated with primary antibodies overnight at either 4°C or RT. Primary antibody concentrations can be found in Table 2. Following primary antibody incubation, sections were washed three to four times in PBS before incubation with fluorescently labeled secondary antibodies for 1 h at RT. All antibody diluent consisted of 0–5% donkey or goat serum and 0.2–0.3% Triton X-100 in PBS. Species-specific secondary antibodies were acquired from either Jackson ImmunoResearch or Thermo Fisher Scientific and were raised in either donkey, goat, or bovine. Secondary antibodies were conjugated to either Alexa Fluor 488 (used at 1:1000), Alexa Fluor 546 (1:500), Cy3 (1:500), or Alexa Fluor 647 (1:200). After secondary antibody incubation, sections were washed three to four times in PBS before mounting in either Vectashield antifade mounting media with DAPI (Vector Laboratories) or Prolong Gold antifade mounting media with DAPI (Thermo Fisher Scientific).

For detection of EdU, sections were removed from the secondary antibody incubation, washed three times in PBS, and incubated for 30 min at RT in a homemade Click reaction mixture containing 4 mM CuSO<sub>4</sub>·5H<sub>2</sub>O (Sigma), 4  $\mu$ M Alexa Fluor-647-conjugated azide (ThermoFisher), and 100 mM sodium ascorbate (Sigma) in Tris buffered saline pH 7.15. Following this, sections were washed in 3% BSA in PBS twice followed by one wash in PBS. Sections were then counterstained with Hoechst's 33342 before being mounted using Vectashield without DAPI (Vector Laboratories).

For myelin staining, Fluoromyelin Red (Invitrogen) was used on cryostat sections from tissue perfused as described above that had been additionally subjected to an overnight postfixation, before cryoprotection and embedding. Staining was performed following the manufacturer's supplied protocol.

#### Image acquisition and analysis

Images were primarily captured using a Nikon A1R Confocal with either a Plan Apo VC 60 $\times$ /1.4 oil objective, a Plan Fluor 40 $\times$ /1.3 oil objective, or a Plan Apo  $\lambda$  20 $\times$ /0.75 objective. Some images were collected using a Leica SP8 Confocal with either a Plan Apo HC 20 $\times$ /0.75 or Plan Apo HC 40 $\times$ /1.30 oil objective. Images for EdU pulse chase analysis and GST $\pi$  labeling were captured on a Zeiss Axiovert 200 M with attached Apotome using either a Plan Apochromat 20 $\times$ /0.75 objective or Plan NeoFluar 40 $\times$ /1.3 oil objective. Image analysis and manipulation was performed using the FIJI distribution of ImageJ (Schindelin et al., 2012).

For quantification of cell density and proportion, we used confocal or Apotome z-stacks collected from the dorsal column region. The boundaries of the dorsal column were outlined and used to calculate total volume of the counted region. The number of immunoreactive cells

for each count was divided by the volume (in  $\text{mm}^3$ ) to calculate density. To calculate the percentage of PLP/DM20+ cells with premyelinating morphology, we collected confocal z-stacks from the dorsal horn spinal cord gray matter and scored cells as either myelinating or premyelinating based on the number and complexity of their processes as well as whether they appeared to contact and form sheaths around axons, using the CC1 antibody to Quaking 7 (QKI7; Bin et al., 2016) to positively identify OLs. It is important to note that the different stages of OL development represent a continuous progression rather than clearly defined states; therefore, cells were scored based on their overall morphology, and some cells were excluded where it was not possible to definitively identify their developmental state.

To measure the fluorescence intensity of Fyn and p416 SFK in GFP+/QKI7+ and GFP-/QKI7+ OLs, we visually divided the dorsal column into three component white matter tracts: the corticospinal tract, the cuneate fasciculus, and the gracile fasciculus. Using a Plan Fluor 40 $\times$ /1.3 oil objective and a z-step size of 0.25  $\mu\text{m}$ , we collected one z-stack from each subregion for each animal. We then selected 20 z-frames from each stack to create maximum projection images. Using the maximum projection images, we drew region of interest (ROI)'s around three GFP+/QKI7+ cells and three GFP-/QKI7+ cells in each image. To restrict analysis just to the outer border of each cell, a smaller ROI was created 10 pixels inside the first ROI. We then combined the two ROIs with the XOR operator to generate a donut-shaped final ROI. This final ROI was used to measure the fluorescence intensity of Fyn or p416 SFK on summed projection images constructed from the original 20 z-frames (each frame's fluorescence intensity was summed into a single projection image). Additional details for specific images or analyses can be found in the figure legends.

#### Experimental design and statistical analysis

In all cases, experiments were designed to compare either iBot<sup>tg/+</sup> with iBot<sup>+/+</sup> animals or GFP+ (BoNT/B-LC reporter) versus GFP- cells in iBot<sup>tg/+</sup> animals. In one case, comparisons were made both among GFP+ and GFP- cells as well as among iBot-expressing and control animals (% ASPA+ OLs). For statistical testing, all comparisons between two groups were conducted using Welch's two sample *t* test with a significance cutoff of  $p < 0.05$ . For qPCR and Western blot analysis data, individual *t* tests were used to compare iBot-expressing and control animals for each gene/protein. For comparison of three or more groups (Fig. 4E), one-way or two-way ANOVA was performed followed by Tukey's HSD *post hoc* testing. Statistical analysis and graphing were performed in R (R Core Team, 2021) using R studio (RStudio Team, 2021) or GraphPad Prism v9. The tidyverse package for R was used for data organization and graph generation (Wickham et al., 2019). Additional details for specific statistical tests are described in the figure legends.

## Results

### Expression of BoNT/B-LC in NG2+ cells and their progeny

To block the function of VAMP2/3 in the developing OL lineage, we crossed heterozygous iBot mice (iBot<sup>tg/+</sup>) expressing cre-dependent BoNT/B-LC and an IRES-linked EGFP reporter (Slezak et al., 2012) with homozygous NG2cre mice (NG2cre<sup>tg/tg</sup>; Fig. 1A; Zhu et al., 2011). In offspring heterozygous for the iBot transgene (referred to as iBot<sup>tg/+</sup> mice), GFP expression was observed in OL lineage cells throughout the spinal cord in both gray and white matter. In the spinal cord dorsal column at P13, immunofluorescence staining for the OPC-specific marker PDGFR $\alpha$  (Fig. 1B1) showed that 84.6  $\pm$  3.7% of PDGFR $\alpha$ + OPCs were GFP+, indicating that BoNT/B-LC was expressed in a majority of immature OPCs during development. To identify early and mature OLs, we labeled with the CC1 monoclonal antibody that detects Quaking 7 (QKI7; Fig. 1B2; Bin et al., 2016). Here, we saw that only 46.4  $\pm$  4.0% of QKI7+ OLs were GFP+, suggesting that a larger than expected fraction of OLs observed at this time point were derived from nonrecombined OPCs. In order to assess the functional expression of BoNT/B in the iBot<sup>tg/+</sup> mice we performed Western blotting for VAMP3 in spinal cord

lysates from iBot<sup>+/+</sup> and iBot<sup>tg/+</sup> mice (Fig. 1C). Normalizing the VAMP3 signal to GAPDH (glyceraldehyde-3-phosphate dehydrogenase), we observed a significant reduction in the amount of intact VAMP3 in the iBot<sup>tg/+</sup> samples ( $2.76 \times 10^3 \pm 586.16$  a.u.) compared with controls ( $8.04 \times 10^3 \pm 498.40$  a.u.; Fig. 1D), verifying that BoNT/B-LC was both expressed and active in the iBot<sup>tg/+</sup> mice.

### VAMP2/3 cleavage in the OL lineage caused severe hypomyelination in the developing mouse spinal cord

Between P10 and P13, iBot<sup>tg/+</sup> mice began exhibiting motor defects which distinguished them from their control, iBot<sup>+/+</sup> littermates. By  $\sim$ P13, these behaviors included impaired limb function, movement difficulties, and difficulty righting themselves, and most of the iBot<sup>tg/+</sup> mice ultimately died between P15 and P17 (Movie 1). Spinal cords harvested from iBot<sup>tg/+</sup> mice frequently appeared more translucent than those from littermate controls, suggesting that the motor impairment may be because of a loss of myelin density (Fig. 1E).

Immunofluorescent staining for MBP in spinal cord sections at P13 showed that iBot<sup>tg/+</sup> animals had patchy, less dense myelin staining compared with controls (Fig. 1F,G). Staining with Fluoromyelin in the dorsal column white matter further indicated a substantial reduction in myelin density in the iBot<sup>tg/+</sup> (Fig. 1I) spinal cord white matter compared with controls (Fig. 1H). Consistent with this, qRT-PCR analysis from whole spinal cord isolate revealed decreased expression of major myelin genes *Mbp*, *Cnp1*, *Plp1*, and *Myrf* in iBot<sup>tg/+</sup> animals relative to controls (Fig. 1J). Western blot analysis of whole spinal cord homogenate similarly showed lower protein levels of MBP (myelin basic protein), CNP (2',3'-cyclic-nucleotide 3'-phosphodiesterase), and PLP (proteolipid protein) but not PDGFR $\alpha$  (Fig. 1K). Together, these results suggested a significant deficiency in either myelin generation or oligodendrocyte differentiation without a major impact on OPCs or their expression of PDGFR $\alpha$ , a key regulator of OPC proliferation and differentiation (Mitew et al., 2014).

### VAMP2/3 cleavage in OPCs significantly reduced the density of QKI7+ OLs but not OPCs

In order to determine whether the myelin deficiency seen in iBot<sup>tg/+</sup> animals was because of a defect in oligodendrocyte differentiation, we measured the density of PDGFR $\alpha$ + OPCs (Fig. 2A,B) and QKI7+ OLs (Fig. 2D,E) in the dorsal column white matter. At P13, we found no significant difference in the density of PDGFR $\alpha$ + cells in iBot<sup>tg/+</sup> animals ( $5.72 \times 10^4 \pm 2.05 \times 10^3$  cells/ $\text{mm}^3$ ) compared with controls ( $4.84 \times 10^4 \pm 6.25 \times 10^3$  cells/ $\text{mm}^3$ ; Fig. 2C); however, the density of early and mature OLs labeled with QKI7 was significantly lower ( $1.37 \times 10^5 \pm 1.47 \times 10^4$  cells/ $\text{mm}^3$  in iBot<sup>tg/+</sup> vs  $2.34 \times 10^5 \pm 1.89 \times 10^4$  cells/ $\text{mm}^3$  in iBot<sup>+/+</sup>; Fig. 2F). The relatively high percentage of PDGFR $\alpha$ + cells expressing GFP ( $\sim$ 85%; Fig. 1C) and the similar density of PDGFR $\alpha$ + cells between iBot<sup>tg/+</sup> animals and controls (Fig. 2C) indicated that this reduction in QKI7+ OLs was not secondary to a loss of OPCs. We therefore reasoned either that developing OLs were being lost after reaching the QKI7+ stage, or that differentiation of OPCs was blocked or impaired. As we did not observe an accumulation of OPCs in the iBot<sup>tg/+</sup> animals, we hypothesized that OPCs were differentiating into QKI7+ OLs but being lost before reaching full maturity.

### OPCs with cleaved VAMP2/3 in iBot<sup>tg/+</sup> mice initiated differentiation, but fewer mature OLs were formed

To assess whether the differentiation of OPCs into newly formed OLs was impaired in the iBot<sup>tg/+</sup> animals, we performed Edu

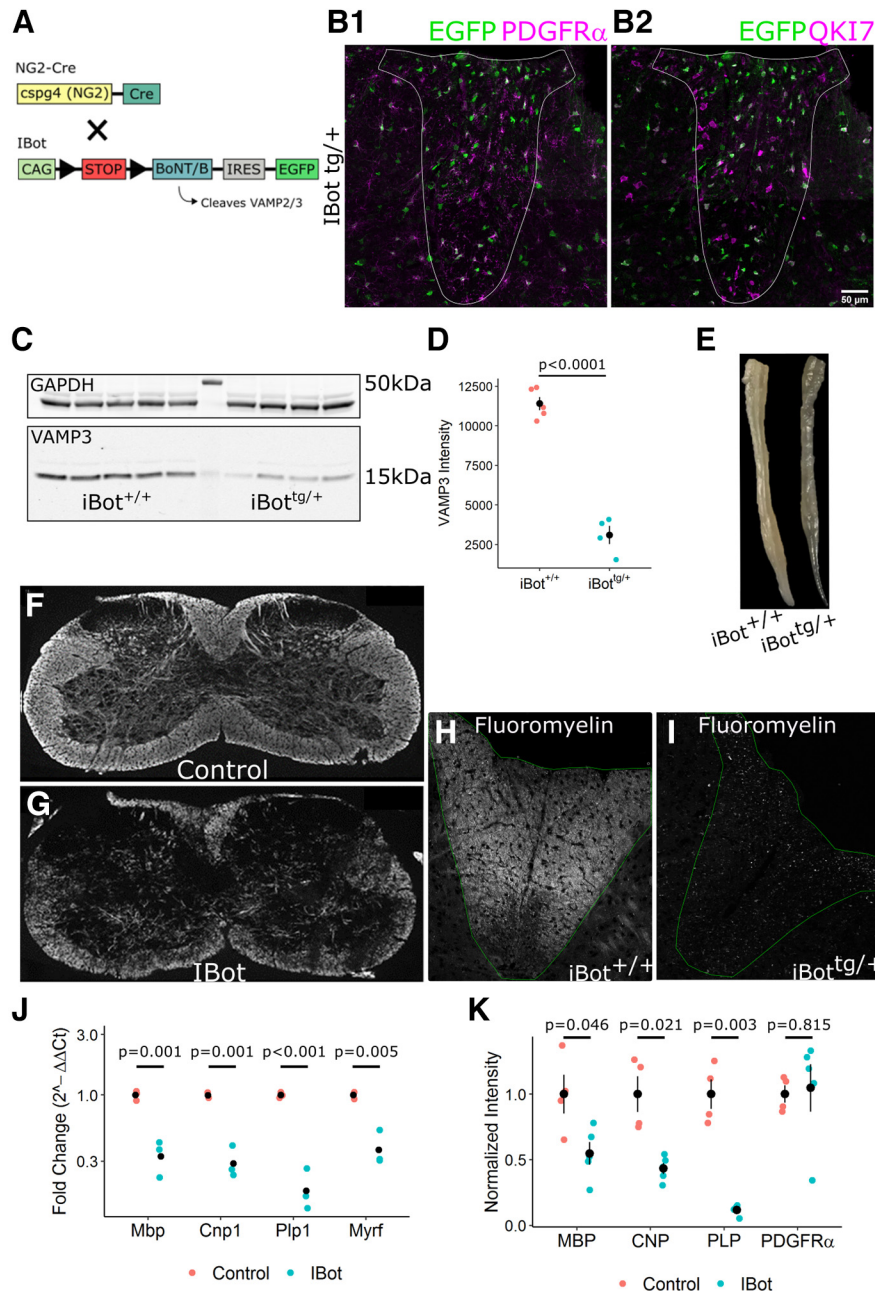


**Figure 1.** Developmental hypomyelination in *iBot*<sup>tg/+</sup> spinal cords. **A**, Schematic of *iBot*<sup>tg/+</sup>NG2cre<sup>tg/+</sup> animals. **B**, P13–P14 *iBot*<sup>tg/+</sup> dorsal column labeled for GFP and PDGFR $\alpha$  (**B1**) or QKI7 (**B2**; scale bar = 50  $\mu$ m). **C**, Western blot analysis for VAMP3 (bottom) and GAPDH (top) from P14–P15 *iBot*<sup>+/+</sup> and *iBot*<sup>tg/+</sup> spinal cord lysate. **D**, Quantification of VAMP3 levels normalized to GAPDH in *iBot*<sup>+/+</sup> ( $8.04 \times 10^3 \pm 498.40$ ) and *iBot*<sup>tg/+</sup> ( $2.76 \times 10^3 \pm 586.16$ ) spinal cords (Welch's two sample *t* test,  $t_{(5.83)} = 11.7$ ,  $p = 2.87 \times 10^{-5}$ ,  $n = 5$  *iBot*<sup>+/+</sup> and 4 *iBot*<sup>tg/+</sup>). **E**, Fixed spinal cords harvested from an *iBot*<sup>+/+</sup> control animal (top) and an *iBot*<sup>tg/+</sup> animal (bottom). **F**, **G**, Cervical spinal cord sections labeled for MBP in *iBot*<sup>+/+</sup> (**F**) and *iBot*<sup>tg/+</sup> animals (**G**). **H**, **I**, Fluoromyelin staining in the dorsal column of P13–P14 *iBot*<sup>+/+</sup> (**H**) and *iBot*<sup>tg/+</sup> (**I**) mice. **J**, qRT-PCR showing decreased expression of *Mbp* (3-fold decrease), *Cnp1* (3.4-fold decrease), *Plp1* (5.4-fold decrease), and *Myrf* (2.6-fold decrease) in *iBot*<sup>tg/+</sup> spinal cords (Welch's two sample *t* test for each gene,  $n = 3$  animals per genotype). Expression values are reported as fold change compared with controls plotted on a log<sub>10</sub> scale. **K**, Western blot analysis showing decreased protein levels of MBP (1.8-fold decrease), CNP (2.3-fold decrease), and PLP (8.6-fold decrease) but not PDGFR $\alpha$  in *iBot*<sup>tg/+</sup> animals compared with controls (Welch's two sample *t* test for each protein,  $n = 4$  animals per genotype). Band intensity shown is normalized to control values after normalization to the reference marker GAPDH. See Movie 1 for video demonstrating motor impairment in an *iBot*<sup>tg/+</sup> mouse.

(5-ethynyl-2'-deoxyuridine) pulse chase labeling by injecting animals with EdU at P10 and killing them P13 to follow the fate of OPCs that were proliferating at P10 (Fig. 3A). We then performed immunofluorescent labeling for QKI7 and EdU labeling in spinal cord sections of *iBot*<sup>tg/+</sup> animals (Fig. 3C) and controls (Fig. 3B). The presence of EdU+/QKI7+/GFP+ cells indicated that *iBot*<sup>tg/+</sup> OPCs did successfully differentiate to the QKI7+ early OL stage between P10 and P13 (Fig. 3D, blue arrows). To determine whether the overall number of new QKI7+ OLs produced during the 3-d time course was

affected, we measured the density of EdU+/QKI7+ cells in the dorsal column and found that there was not a significant difference between *iBot*<sup>tg/+</sup> animals ( $1.67 \times 10^4 \pm 4.97 \times 10^3$  cells/mm<sup>3</sup>) and controls ( $1.82 \times 10^4 \pm 6.16 \times 10^3$  cells/mm<sup>3</sup>; Fig. 3E) despite significantly fewer QKI7+ OLs overall (Fig. 2F). This further indicated that the reduction in OL number seen in *iBot*<sup>tg/+</sup> mice was not because of a failure of OPCs to generate new QKI7+ OLs, supporting the interpretation that VAMP2/3 deficiency primarily affects developing OLs after they have reached the QKI7+ early OL stage.



**Movie 1.** Example video of a representative  $iBot^{tg/+}$  mouse at P13 demonstrating severely impaired coordination and motor function, followed by a control P13 mouse for comparison starting at 27 s. [View online]

We tested this possibility further using immunofluorescent labeling for QKI7 in combination with the mature OL marker glutathione S-transferase  $\pi$  (GST $\pi$ ; Tansey and Cammer, 1991). QKI7+/GST $\pi$ + cells were considered to be mature OLs, while QKI7+/GST $\pi$ - cells were considered newly formed, early OLs. Consistent with the overall reduction in QKI7+ cell density (Fig. 2F),  $iBot^{tg/+}$  animals showed fewer GST $\pi$ + OLs (Fig. 4B) than controls (Fig. 4A). Additionally, the proportion of QKI7+ cells that were GST $\pi$ + was significantly lower in  $iBot^{tg/+}$  animals ( $31.3 \pm 3.6\%$ ) compared with controls ( $56.6 \pm 1.0\%$ ; Fig. 4C) suggesting that, despite reaching the QKI7+ stage, fewer early OLs were successfully reaching full maturity in the  $iBot^{tg/+}$  animals.

Using another marker for mature OLs, aspartoacylase (ASP; Pan et al., 2020), we next tested whether the failure to reach a fully mature stage was restricted to those cells expressing BoNT/B-LC, identified as GFP+ cells. In control animals, we found that the proportion of QKI7+ cells that were also ASP+ ( $58.4 \pm 2.5\%$ ; Fig. 4D) was similar to that seen with GST $\pi$  ( $56.6 \pm 1.0\%$ ; Fig. 4D), confirming that the timing of expression for these two markers was similar in OL lineage development. In  $iBot^{tg/+}$  animals, the proportion of GFP+/QKI7+ cells labeled by ASPA was significantly lower ( $10.6 \pm 4.7\%$ ) compared with the proportion of QKI7+ cells that were ASPA+ in control animals ( $58.4 \pm 2.5\%$ ) and to the proportion of GFP-/QKI7+ cells that were ASPA+ sampled from  $iBot^{tg/+}$  animals ( $41.3 \pm 8.0\%$ ; Fig. 4D). This confirmed that fewer newly differentiated BoNT/B-expressing OLs were becoming fully mature in the  $iBot^{tg/+}$  animals. In addition, this result suggested that VAMP2/3 deficiency impairs OL lineage development cell autonomously, as the proportion of GFP- OLs expressing ASPA in  $iBot^{tg/+}$  mice was not significantly reduced compared with controls.

#### Vamp2 knock-down impaired OL maturation in culture

To verify that the OL maturation defect observed in  $iBot^{tg/+}$  spinal cord was because of loss of intact VAMP2/3, we used lentiviral vectors encoding Vamp2 or Vamp3 shRNA-GFP to knock-down VAMP2 or VAMP3 in dissociated cultures enriched in OPCs from perinatal rat spinal cords. Following transduction, the cells were kept in differentiation media for 6 d and immunolabeled for MBP (Fig. 4E–G). Cells infected with control-GFP lentivirus displayed the most mature OL morphology, represented by lamellar

morphology consisting of wide membranous expansion of MBP+ processes (Pfeiffer et al., 1993; Zuchero et al., 2015; Fig. 4E). By contrast, cells transduced with Vamp2shRNA-GFP lentivirus had the most immature morphology, with many of the cells exhibiting simple radial or oligopolar morphology (Fig. 4F). Cells transduced with Vamp3shRNA-GFP appeared less differentiated than control-GFP-transduced cells but more mature than Vamp2shRNA-GFP-transduced cells, with some membranous expansions forming in distal processes (Fig. 4G). We determined the proportion of GFP+ MBP+ mature OLs that exhibited membranous expansion of MBP reactivity (Fig. 4H). Transduction with Vamp2shRNA significantly reduced the proportion of mature OLs to a level 3.7-fold lower than control-GFP-transduced cells. Vamp3 knock-down led to a 2-fold reduction in the proportion of mature OLs, but the effect did not reach significance at  $\alpha = 0.05$ . These findings indicate that loss of cleavage of VAMP2 impairs OL maturation in a cell-autonomous manner. We also noted that the density of cells treated with Vamp2shRNA lentivirus was lower than that of cultures treated with control-GFP or Vamp3shRNA-GFP lentivirus, and many Vamp2shRNA-transduced GFP+ MBP+ cells were smaller, suggesting that VAMP2-dependent processes play a critical role in OL survival.

#### Impaired re-upregulation of NKX2.2 in $iBot^{tg/+}$ spinal cord during myelination

In order to better determine the stage of differentiation at which  $iBot^{tg/+}$  OLs are affected, we labeled for NKX2.2, a transcription factor involved in the regulation of OL differentiation and maturation that is upregulated in OPCs just before the onset of differentiation and then rapidly downregulated as they approach the final stages of differentiation (Qi et al., 2001; Watanabe et al., 2004). Following a period of downregulation in newly-mature OLs, however, it has been shown that NKX2.2 is eventually re-expressed at lower levels (Cai et al., 2010; see Fig. 10 for a diagram summarizing gene expression timing). Consistent with this, NKX2.2 labeling in the dorsal column of  $iBot^{+/+}$  spinal cords showed a mixture of both highly-expressing NKX2.2+ cells, corresponding to actively differentiating OLs (referred to as NKX2.2<sup>high</sup> OLs), and weakly-expressing NKX2.2+ cells, corresponding to mature OLs that have reacquired NKX2.2 expression (referred to as NKX2.2<sup>low</sup> OLs; Fig. 5A). In comparison, in the dorsal column of  $iBot^{tg/+}$  mice we observed an apparent reduction in the overall density of NKX2.2+ cells as well as a relative lack of weakly-expressing NKX2.2<sup>low</sup> cells (Fig. 5B). When we quantified the overall density of NKX2.2+/QKI7+ OLs, using QKI7 to exclude NKX2.2+ OPCs, we found that the density was significantly reduced in the  $iBot^{tg/+}$  mice ( $2.08 \times 10^4 \pm 2.30 \times 10^3$  cells/mm<sup>3</sup>) relative to controls ( $3.93 \times 10^4 \pm 1.80 \times 10^3$  cells/mm<sup>3</sup>; Fig. 5C). However, when we similarly quantified only the NKX2.2<sup>high</sup>/QKI7+ OLs we found that the density was not significantly affected in  $iBot^{tg/+}$  mice ( $1.33 \times 10^4 \pm 2.42 \times 10^3$  cells/mm<sup>3</sup>) relative to controls ( $9.29 \times 10^3 \pm 263.90$  cells/mm<sup>3</sup>; Fig. 5D). This suggested that the number of actively differentiating OLs was unchanged but that the number of NKX2.2<sup>low</sup> mature OLs was reduced in the  $iBot^{tg/+}$  mice, further supporting the interpretation that  $iBot^{tg/+}$  OLs proceed successfully through the initial stages of differentiation but either stall or undergo cell death before completing the maturation processes.

To confirm that the NKX2.2<sup>low</sup> cells observed were fully differentiated OLs, we double labeled for NKX2.2 and ASPA as a marker for mature OLs. In  $iBot^{+/+}$  control mice, we found that many of the NKX2.2<sup>low</sup> cells were also ASPA+, confirming they were fully mature OLs, while the NKX2.2<sup>high</sup> cells were almost

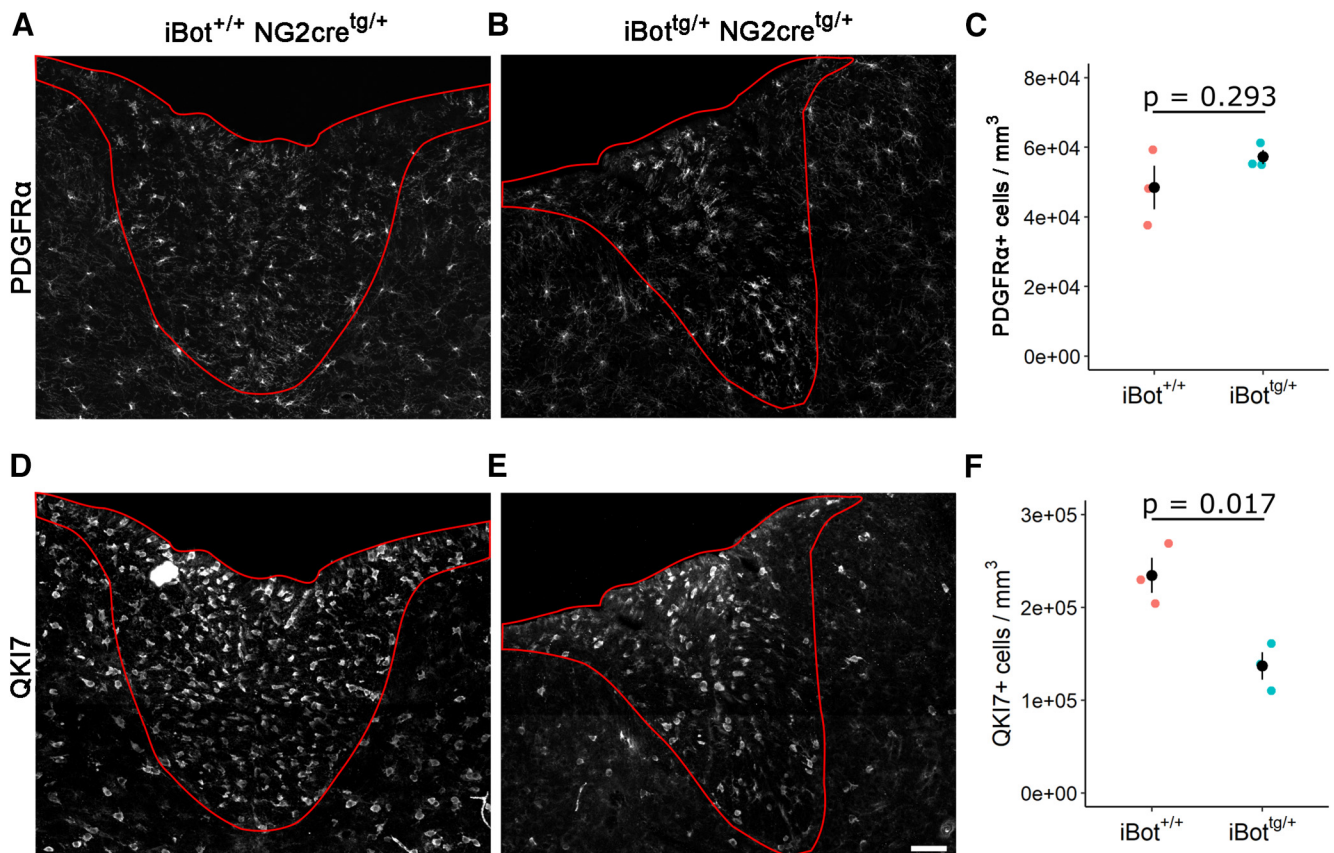


**Figure 2.** Density of PDGFR $\alpha$ + OPCs and QKI7+ OLs in the dorsal column. **A, B**, PDGFR $\alpha$  labeling in P13–P14 iBot<sup>+/+</sup> (**A**) and iBot<sup>tg/+</sup> (**B**) dorsal column. **C**, PDGFR $\alpha$ + cell density in iBot<sup>tg/+</sup> dorsal column ( $5.72 \times 10^4 \pm 2.05 \times 10^3$  cells/mm<sup>3</sup>) and control iBot<sup>+/+</sup> dorsal column ( $4.84 \times 10^4 \pm 6.25 \times 10^3$  cells/mm<sup>3</sup>, Welch's two sample *t* test,  $t_{(2,43)} = -1.338$ ,  $p = 0.293$ ,  $n = 3$  animals for each genotype). **D, E**, QKI7 labeling in P13–P14 iBot<sup>+/+</sup> (**D**) and iBot<sup>tg/+</sup> (**E**) dorsal column. **F**, QKI7+ cell density in iBot<sup>tg/+</sup> dorsal column ( $1.37 \times 10^5 \pm 1.45 \times 10^4$  cells/mm<sup>3</sup>) and control iBot<sup>+/+</sup> dorsal column ( $2.34 \times 10^5 \pm 1.89 \times 10^4$  cells/mm<sup>3</sup>, Welch's two sample *t* test,  $t_{(3,77)} = 4.074$ ,  $p = 0.017$ ,  $n = 3$  animals for each genotype).

entirely ASPA<sup>−</sup>, indicating they were either immature, actively differentiating OLs or committed OPCs (Fig. 5E). When we quantified the percentage of ASPA<sup>+</sup> OLs that co-expressed NKX2.2 we found that it was significantly lower in the iBot<sup>tg/+</sup> mice ( $10.53 \pm 2.83\%$ ) compared with controls ( $31.06 \pm 3.05\%$ ), suggesting a reduced accumulation of mature OLs in the developing iBot<sup>tg/+</sup> spinal cord (Fig. 5F). Similarly, using double labeling for QKI7 and NKX2.2 in iBot<sup>+/+</sup> and iBot<sup>tg/+</sup> dorsal column (Fig. 5G,H), we found that the percentage of QKI7+ OLs co-expressing NKX2.2 was also significantly reduced in iBot<sup>tg/+</sup> mice ( $27.60 \pm 1.05\%$  vs  $33.68 \pm 0.90\%$  in control mice; Fig. 5I). As ASPA<sup>+</sup> OL are also QKI7<sup>+</sup>, the milder reduction in the proportion of NKX2.2+ OLs among total QKI7+ OLs likely also reflects a reduced or slowed developmental accumulation of mature OLs reacquiring NKX2.2 expression. Notably, however, the percentage of QKI7+ OLs that were NKX2.2<sup>high</sup> was not reduced, instead showing a trend toward an increased percentage of NKX2.2<sup>high</sup>/QKI7+ OLs in the iBot<sup>tg/+</sup> mice (Fig. 5J), suggesting that the iBot<sup>tg/+</sup> OLs may undergo cell death, removing them from the total QKI7+ population, following the initial downregulation of NKX2.2 in the final stages of differentiation but before its re-expression in fully mature OLs.

#### Survival of OLs appeared reduced in the dorsal column of iBot<sup>tg/+</sup> animals

To further investigate the fate of differentiating iBot<sup>tg/+</sup> OLs, we performed immunofluorescent staining for cleaved caspase 3 (cCasp3), a marker for cells undergoing apoptosis, to determine

whether their survival was impaired by loss of VAMP2/3 function. At P13, we found that the density of cCasp3+ cells in the dorsal column was significantly higher in iBot<sup>tg/+</sup> mice ( $4.45 \times 10^3 \pm 992.8$  cells/mm<sup>3</sup>) compared with iBot<sup>+/+</sup> control mice ( $1.64 \times 10^3 \pm 429.9$  cells/mm<sup>3</sup>; Fig. 6C), though it is worth noting that few cCasp3+ cells were detected overall in either iBot<sup>tg/+</sup> or control animals (range of zero to nine cCasp3+ cells per dorsal column sampled; Fig. 6A,B). To assess whether the cCasp3+ cells in iBot<sup>tg/+</sup> animals belonged to the OL lineage, we then labeled for cCasp3 and for Olig2, a marker expressed throughout the OL lineage (Fig. 6A,B). We found that there was a trend toward increased cCasp3+/Olig2+ cell density in iBot<sup>tg/+</sup> mice ( $3.89 \times 10^3 \pm 1.59 \times 10^3$  cells/mm<sup>3</sup>) compared with controls ( $868.8 \pm 369.6$  cells/mm<sup>3</sup>; Fig. 6D); however, this difference was not statistically significant. Preliminary TUNEL staining performed at P8 similarly suggested enhanced cell death in the iBot<sup>tg/+</sup> mice (data not shown).

In order to assess the contribution of astrocytes undergoing apoptosis to the overall cCasp3+ cell density, we also performed immunofluorescent labeling with cCasp3 and the astrocyte marker ALDH1L1. The lack of cCasp3+/ALDH1L1+ astrocytes in iBot<sup>tg/+</sup> animals indicated that apoptotic astrocytes did not contribute significantly to the overall cCasp3+ cell density (Fig. 6E). Similarly, when we labeled with cCasp3 and the microglial marker Iba1, we detected no cCasp3+/Iba1+ microglia in the dorsal columns of iBot<sup>tg/+</sup> animals (not shown). Comparison of cCasp3 staining with GFP expression in iBot<sup>tg/+</sup> animals showed that 75.7% of cCasp3+ cells were also GFP+, suggesting that the

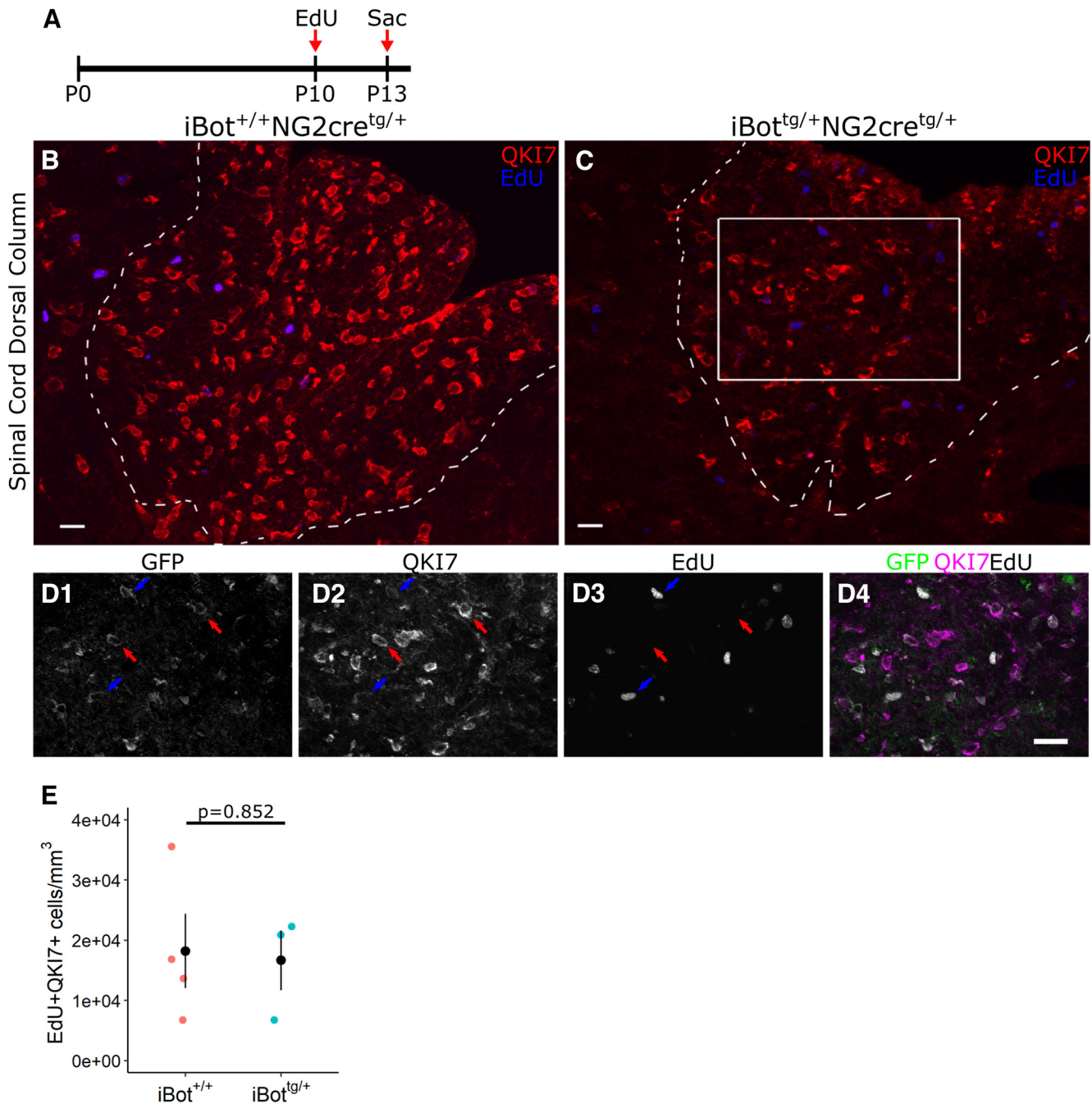


**Figure 3.** EdU pulse chase labeling of *iBot*<sup>tg/+</sup> and control animals from P10–P13. **A**, Schematic illustrating design of EdU pulse chase experiment. **B**, **C**, Double label for QKI7 and EdU in P13 *iBot*<sup>+/+</sup> (**B**) and *iBot*<sup>tg/+</sup> (**C**) dorsal column. **D**, Labeling for GFP, QKI7, and EdU from the area marked in **C** showing GFP+/QKI7+/EdU– OLs (red arrows) and GFP+/QKI7+/EdU+ OLs (blue arrows). **E**, EdU+/QKI7+ cell density in *iBot*<sup>+/+</sup> ( $1.82 \times 10^4 \pm 6.16 \times 10^3$  cells/mm<sup>3</sup>) and *iBot*<sup>tg/+</sup> dorsal column ( $1.67 \times 10^4 \pm 4.97 \times 10^3$  cells/mm<sup>3</sup>, Welch's two sample *t* test, *t*<sub>(5)</sub> = 0.196, *p* = 0.852, *n* = 4 *iBot*<sup>+/+</sup> and 3 *iBot*<sup>tg/+</sup> animals). Scale bars = 20 μm (**B**, **C**), 25 μm (**D**).

majority of cCasp3+ cells were derived from NG2+ progenitors (Fig. 6F). Taken together, these results suggest that the *iBot*<sup>tg/+</sup> OLs that fail to reach maturity eventually undergo cell death resulting in the reduced density of QKI7+ OLs seen in the *iBot*<sup>tg/+</sup> mice.

#### At P13, fewer *iBot*<sup>tg/+</sup> OLs display morphologic features of mature, myelinating OLs

In the early OL phase, developing OLs begin expressing *Qki* and initially adopt a morphology that is distinct from more mature, myelinating OLs. OLs with a typical premyelinating morphology

are characterized by numerous, highly-branched processes that extend radially from the soma. In contrast, myelinating OLs have fewer, less complex processes which extend toward and contact axons to form myelin sheaths (Butt et al., 1997).

To assess whether *iBot*<sup>tg/+</sup> OLs underwent the stereotypical transition from premyelinating to myelinating morphology despite lacking the expression profile of fully mature OLs, we used an anti-PLP antibody, referred to by its clone name AA3 (Yamamura et al., 1991), that reacts with both PLP and the DM20 splice variant, to compare the morphologic characteristics of GFP+ and GFP– OLs in *iBot*<sup>tg/+</sup> spinal cords. Here, we



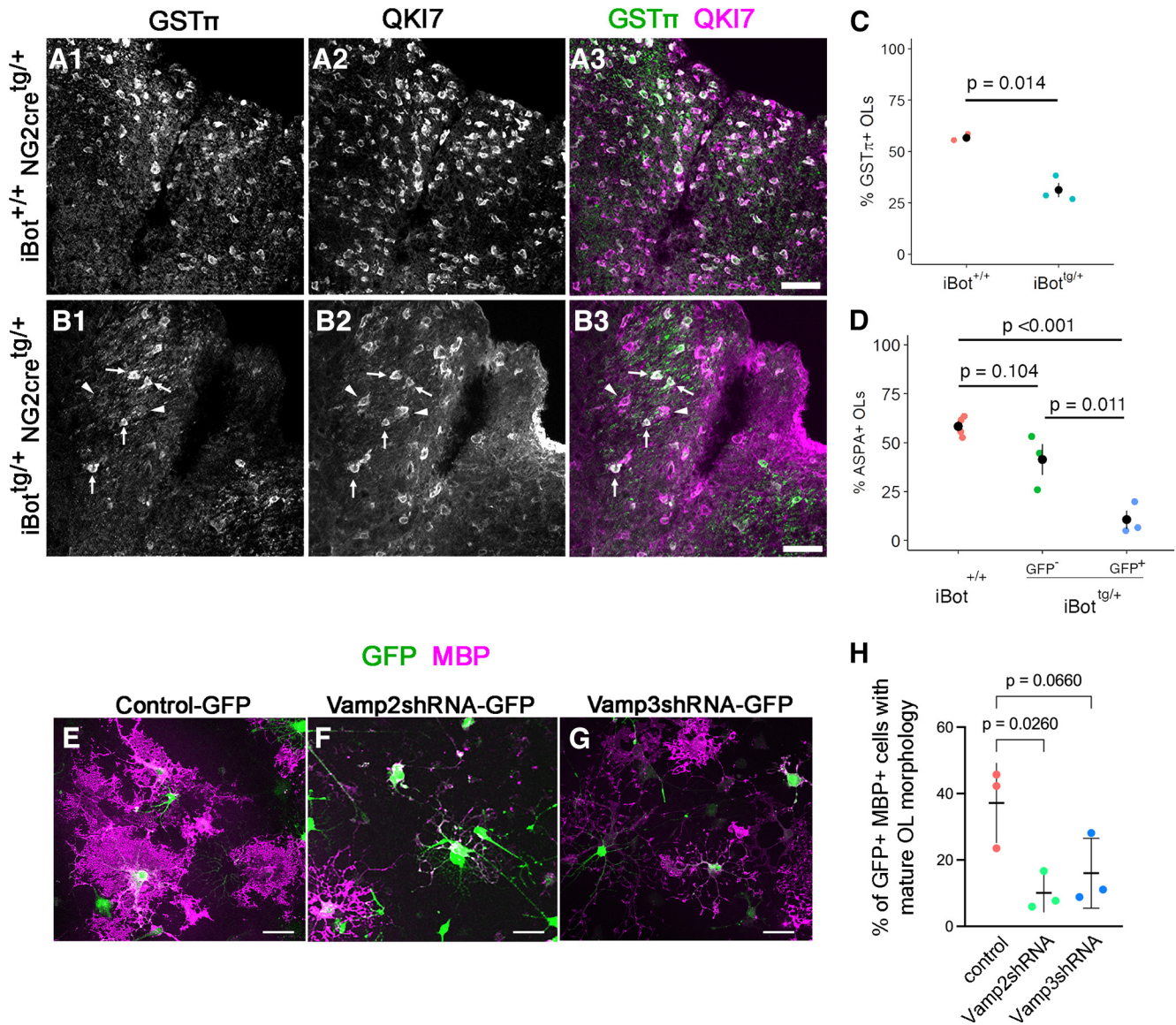


**Figure 4.** Defective OL maturation in P13–P14 iBot<sup>tg/+</sup> dorsal column and following Vamp2/3 knock-down. **A, B**, Labeling for GST $\pi$  and QKI7 at P13 in iBot<sup>+/+</sup> (**A**) and iBot<sup>tg/+</sup> dorsal column (**B**). Arrowheads in **B** show QKI7+/GST $\pi$ -negative early OLs, and arrows show QKI7+/GST $\pi$ + mature OLs. **C**, Percentage of QKI7+ OLs also labeled by GST $\pi$  in iBot<sup>tg/+</sup> (31.3 ± 3.6%) and iBot<sup>+/+</sup> dorsal column (56.6 ± 1.0%, Welch's two sample *t* test,  $t_{(2,33)} = 6.856$ ,  $p = 0.014$ ,  $n = 3$  animals for each genotype). **D**, Percentage of QKI7+ OLs that were ASPA+ at P13–P14 in iBot<sup>+/+</sup> dorsal column (58.4 ± 2.5%), among GFP<sup>-</sup> cells in iBot<sup>tg/+</sup> dorsal column (41.3 ± 8.0%), and among GFP+ cells in iBot<sup>tg/+</sup> dorsal column (10.6 ± 4.7%, ANOVA,  $F_{(2,7)} = 23.07$ ,  $p = 8.30 \times 10^{-4}$ , Tukey's HSD *post hoc* tests,  $p = 6.55 \times 10^{-4}$  for iBot<sup>+/+</sup>:iBot<sup>tg/+</sup>GFP+). **E–G**, Dissociated rat spinal cord OPCs transduced with lentivirus encoding control-GFP (**E**), Vamp2shRNA-GFP (**F**), or Vamp3shRNA-GFP (**G**) and stained for MBP after 6 d in differentiation media. **H**, Proportion of MBP+ GFP+ cells with mature OL morphology, exhibiting membranous processes. One-way ANOVA, Brown–Forsythe test,  $F_{(2,6)} = 6.340$ ,  $p = 0.0331$ . Scale bars = 50  $\mu$ m.

examined OLs in the dorsal horn gray matter region where myelinated fibers are sparser, allowing us to visualize the morphology of individual cells more easily. Using QKI7 to identify both early and mature OLs in iBot<sup>tg/+</sup> animals, we observed that GFP+/QKI7+ cells (OLs expressing BoNT/B-LC) could be found with both typical premyelinating morphology (Fig. 7A) as well as more mature morphology indicative of myelination (Fig. 7B) and comparable to GFP-/QKI7+ control cells (Fig. 7C). This suggested that functional loss of VAMP2/3 did not uniformly block morphologic maturation of iBot<sup>tg/+</sup> OLs; however, we also found that a significantly higher percentage of GFP+/QKI7+ OLs had a premyelinating morphology (46.4 ± 6.9%) when compared with GFP-/QKI7+ OLs from the same animals (0%; Fig. 6D). Consistent with this, iBot<sup>tg/+</sup> animals appeared to have an expanded population of premyelinating OLs in the

dorsal horn compared with controls (Fig. 6E,F). Given that the number of newly formed QKI7+ OLs was unaffected in iBot<sup>tg/+</sup> animals (Figs. 3E, 5D), the increased prevalence of premyelinating cells among GFP+ OLs suggested that these cells may undergo an extended premyelinating stage, which could contribute to their ultimate failure to reach full maturity.

#### Early OLs with cleaved VAMP2/3 exhibited significantly higher levels of Src kinase Fyn

We next wanted to investigate key signaling pathways known to regulate OL maturation that could be affected in the iBot<sup>tg/+</sup> mice. As the differentiating iBot<sup>tg/+</sup> OLs appeared to stall in the premyelinating stage around the onset of myelination, we looked for signaling factors that would be actively contributing to the regulation of this process. The nonreceptor tyrosine kinase Fyn,

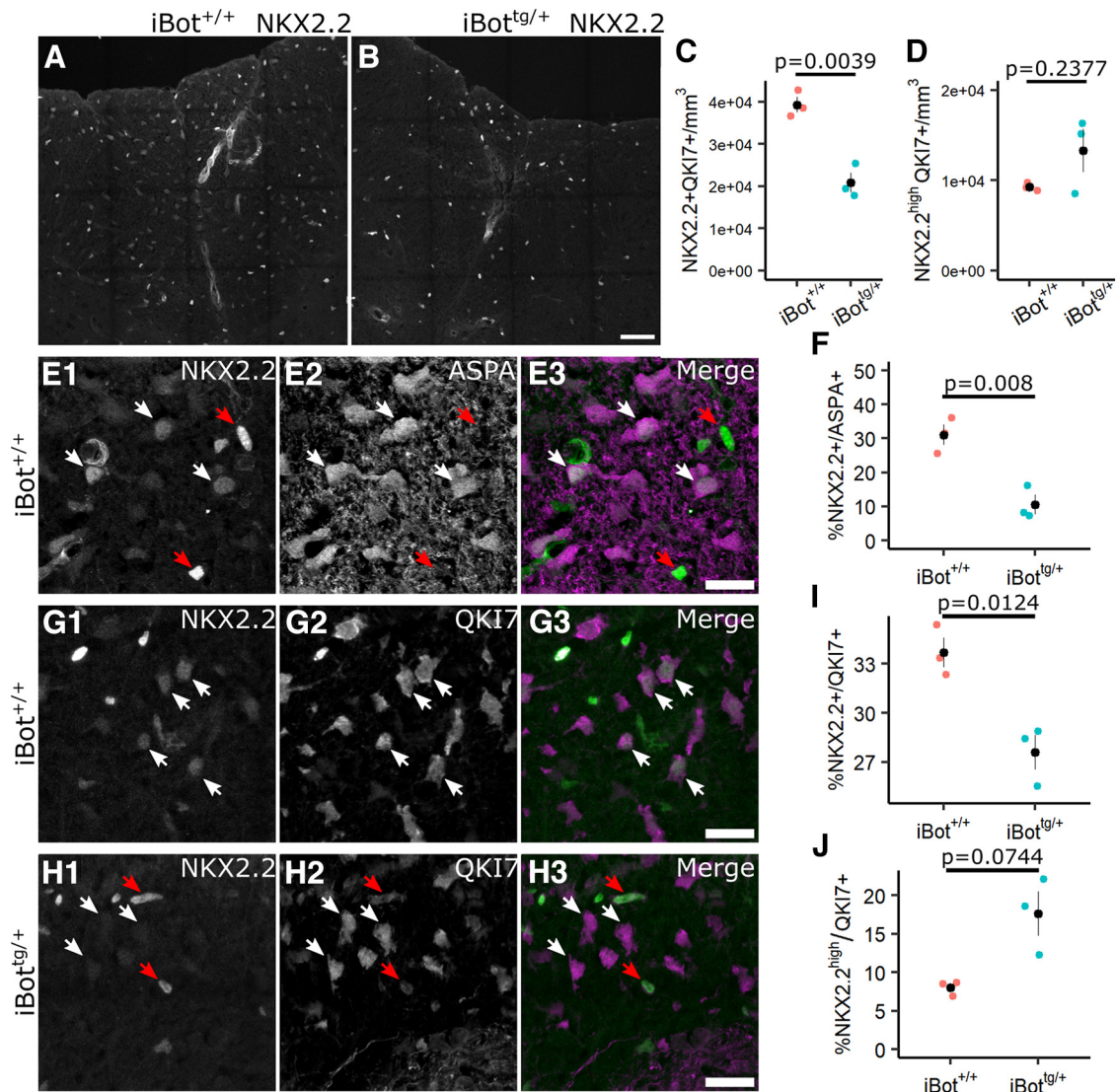


**Figure 5.** Expression of NKX2.2 among QKI7+ and ASPA+ OLs in *iBot*<sup>+/+</sup> and *iBot*<sup>tg/+</sup> dorsal column. **A, B**, NKX2.2 labeling in spinal cord sections from P13 to P14 *iBot*<sup>+/+</sup> (**A**) and *iBot*<sup>tg/+</sup> (**B**) mice. **C**, Density of NKX2.2+/QKI7+ cells in dorsal column of *iBot*<sup>+/+</sup> ( $3.93 \times 10^4 \pm 1.80 \times 10^3$  cells/mm<sup>3</sup>) and *iBot*<sup>tg/+</sup> mice ( $2.08 \times 10^4 \pm 2.30 \times 10^3$  cells/mm<sup>3</sup>;  $t_{(3,79)} = 6.31$ ,  $p = 0.0039$ ). **D**, Density of NKX2.2<sup>high</sup>/QKI7+ in dorsal column of *iBot*<sup>+/+</sup> ( $9.29 \times 10^3 \pm 263.90$  cells/mm<sup>3</sup>) and *iBot*<sup>tg/+</sup> mice ( $1.33 \times 10^4 \pm 2.42 \times 10^3$  cells/mm<sup>3</sup>;  $t_{(2,05)} = -1.65$ ,  $p = 0.2377$ ). **E**, Labeling for NKX2.2 and ASPA in the dorsal column of *iBot*<sup>+/+</sup> control mice showing NKX2.2<sup>high</sup>/ASPA+ cells (red arrows) and NKX2.2<sup>low</sup>/ASPA+ cells (white arrows). **F**, Quantification of the percentage of ASPA+ OLs with detectable nuclear NKX2.2 expression in *iBot*<sup>+/+</sup> ( $31.06 \pm 3.05\%$ ) and *iBot*<sup>tg/+</sup> ( $10.53 \pm 2.83\%$ ) dorsal column ( $t_{(3,98)} = 4.93$ ,  $p = 0.008$ ). **G**, Immunofluorescent labeling for NKX2.2 and QKI7 in *iBot*<sup>+/+</sup> dorsal column showing NKX2.2<sup>low</sup> OLs (white arrows). **H**, Labeling for NKX2.2 and QKI7 in *iBot*<sup>tg/+</sup> dorsal column showing NKX2.2<sup>high</sup> (red arrows) and NKX2.2- OLs (white arrows). **I**, Quantification of the percentage of NKX2.2+ QKI7+ OLs in *iBot*<sup>+/+</sup> ( $33.68 \pm 0.90\%$ ) and *iBot*<sup>tg/+</sup> dorsal column ( $27.60 \pm 1.05\%$ ;  $t_{(3,90)} = 4.40$ ,  $p = 0.0124$ ). **J**, Percentage of NKX2.2<sup>high</sup>/QKI7+ OLs in *iBot*<sup>+/+</sup> ( $8.01 \pm 0.55\%$ ) and *iBot*<sup>tg/+</sup> dorsal column ( $17.64 \pm 2.88\%$ ;  $t_{(2,15)} = -3.28$ ,  $p = 0.0744$ ). All statistical tests done using Welch's two sample *t* test with  $n = 3$  animals for each genotype. Scale bars = 50  $\mu$ m (**A, B**), 20  $\mu$ m (**E, G, H**).

a member of the Src family of kinases, has been shown to regulate OL lineage cell survival and maturation and is thought to be particularly important for mediating axon-OL signaling (Laursen et al., 2009; White and Krämer-Albers, 2014). In addition, recent scRNA-Seq data from OL lineage cells has shown that *Fyn* expression in the OL lineage is highly enriched in the late OPC/early OL stage and begins to decline as expression of major myelin associated genes like *Mag* and *Mog* increases (Marques et al., 2016; Floriddia et al., 2020). Immunofluorescent labeling for *Fyn* in QKI7+ OLs in the dorsal column of *iBot*<sup>tg/+</sup> mice indicated significantly higher levels of *Fyn* associated with somas of GFP+/QKI7+ cells ( $1.41 \times 10^4 \pm 819.3$  a.u.) compared with GFP-/QKI7+ controls ( $8.61 \times 10^3 \pm 495.1$  a.u.; Fig. 8A,B). This suggested that the *iBot*<sup>tg/+</sup> OLs may exhibit abnormally high levels of *Fyn*, possibly because of an accumulation of *Fyn* protein because of an extended premyelinating stage.

Given that *Fyn* activity generally promotes maturation and myelination in early OLs, the possibility that *iBot*<sup>tg/+</sup> OLs, which fail to reach maturity, showed enhanced levels of *Fyn* expression was surprising. Therefore, we also wanted to determine whether the elevated levels of *Fyn* corresponded to functionally active *Fyn* as well. To test this, we performed similar immunofluorescent labeling with a phospho-specific antibody directed against Src family kinases phosphorylated at Y416 (pY416 SFK; Fig. 8C). *Fyn* is the predominant Src family kinase expressed in the OL lineage and is activated by phosphorylation at pY416 (Matrone et al., 2020). Using QKI7 as a marker for developing and mature OLs, we compared the intensity of pY416 SFK staining around the somas of GFP- and GFP+ OLs in the dorsal column of *iBot*<sup>tg/+</sup> animals and found that, similar to total *Fyn*, GFP+ OLs had significantly stronger pY416 SFK staining ( $1.45 \times 10^4 \pm 1.03 \times$

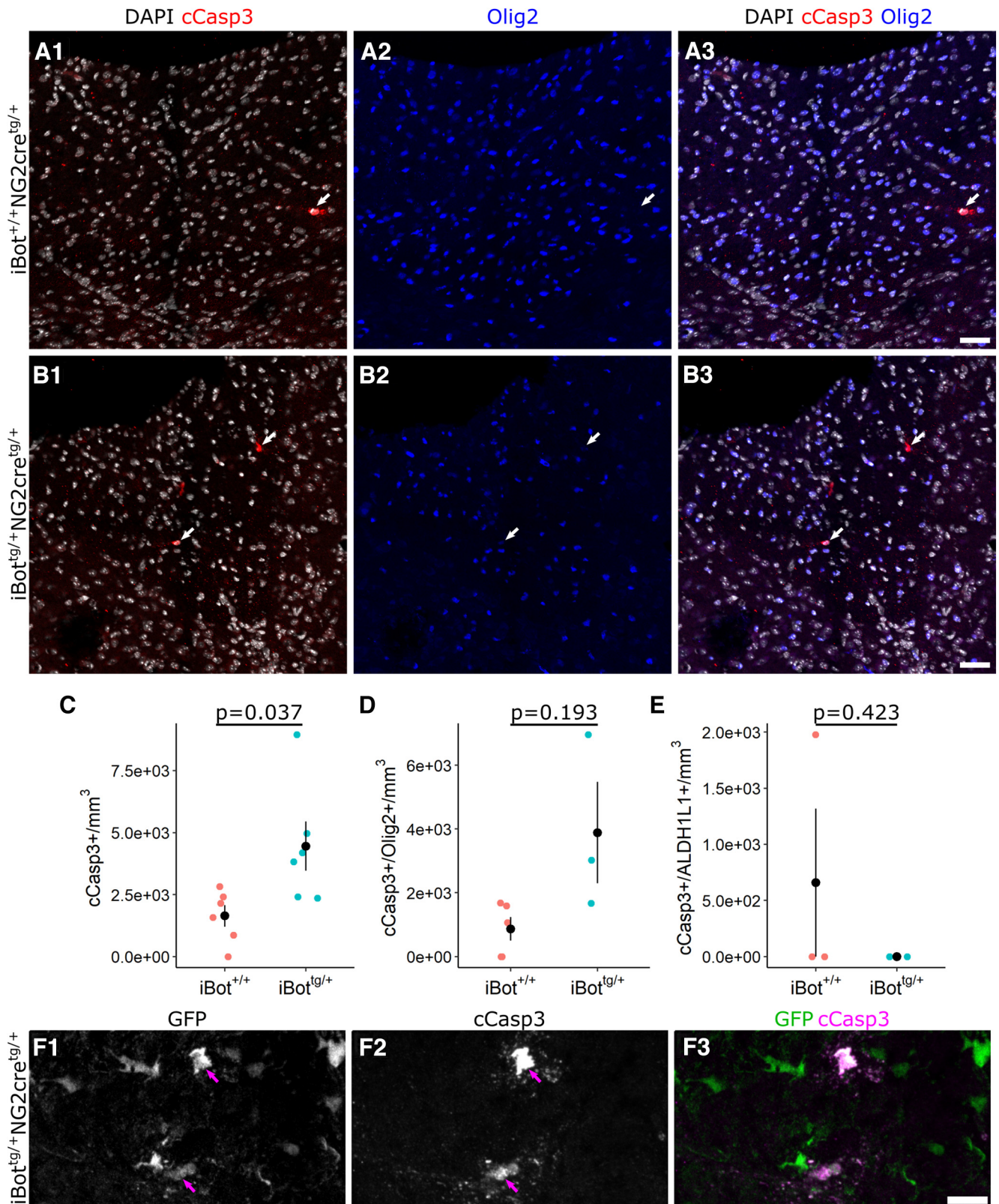


**Figure 6.** Cleaved caspase 3 labeling for apoptotic cells in P13 dorsal column. **A, B**, Double label for cCasp3 and Olig2 with DAPI in dorsal column of P13 iBot<sup>+/+</sup> (**A**) and iBot<sup>tg/+</sup> mice (**B**) showing cCasp3<sup>+</sup> apoptotic cells (arrows). **C**, cCasp3<sup>+</sup> cell density in the dorsal column of P13 iBot<sup>+/+</sup> mice ( $1.64 \times 10^3 \pm 429.9$  cells/mm<sup>3</sup>) and iBot<sup>tg/+</sup> mice ( $4.45 \times 10^3 \pm 992.8$  cells/mm<sup>3</sup>, Welch's two sample *t* test,  $t_{(6,8)} = -2.60$ ,  $p = 0.036$ ,  $n = 6$  iBot<sup>+/+</sup> and 6 iBot<sup>tg/+</sup> animals). **D**, Density of double labeled cCasp3<sup>+</sup>/Olig2<sup>+</sup> cells in the dorsal column of P13 iBot<sup>+/+</sup> mice ( $868.8 \pm 369.6$  cells/mm<sup>3</sup>) and iBot<sup>tg/+</sup> mice ( $3.89 \times 10^3 \pm 1.59 \times 10^3$  cells/mm<sup>3</sup>, Welch's two sample *t* test,  $t_{(2,22)} = -1.852$ ,  $p = 0.193$ ,  $n = 5$  iBot<sup>+/+</sup> and 3 iBot<sup>tg/+</sup> animals). **E**, Density of double labeled cCasp3<sup>+</sup>/ALDH1L1<sup>+</sup> cells in the dorsal column of P13 iBot<sup>+/+</sup> mice ( $659.4 \pm 659.4$  cells/mm<sup>3</sup>) and iBot<sup>tg/+</sup> mice (0 cells/mm<sup>3</sup>, Welch's two sample *t* test,  $t_{(2)} = 1$ ,  $p = 0.4226$ ,  $n = 3$  animals for each genotype). **F**, cCasp3<sup>+</sup>/GFP<sup>+</sup> double labeled cells (arrows) in P13 iBot<sup>tg/+</sup> dorsal column. Scale bars = 50  $\mu$ m (**A, B**), 10  $\mu$ m (**F**).

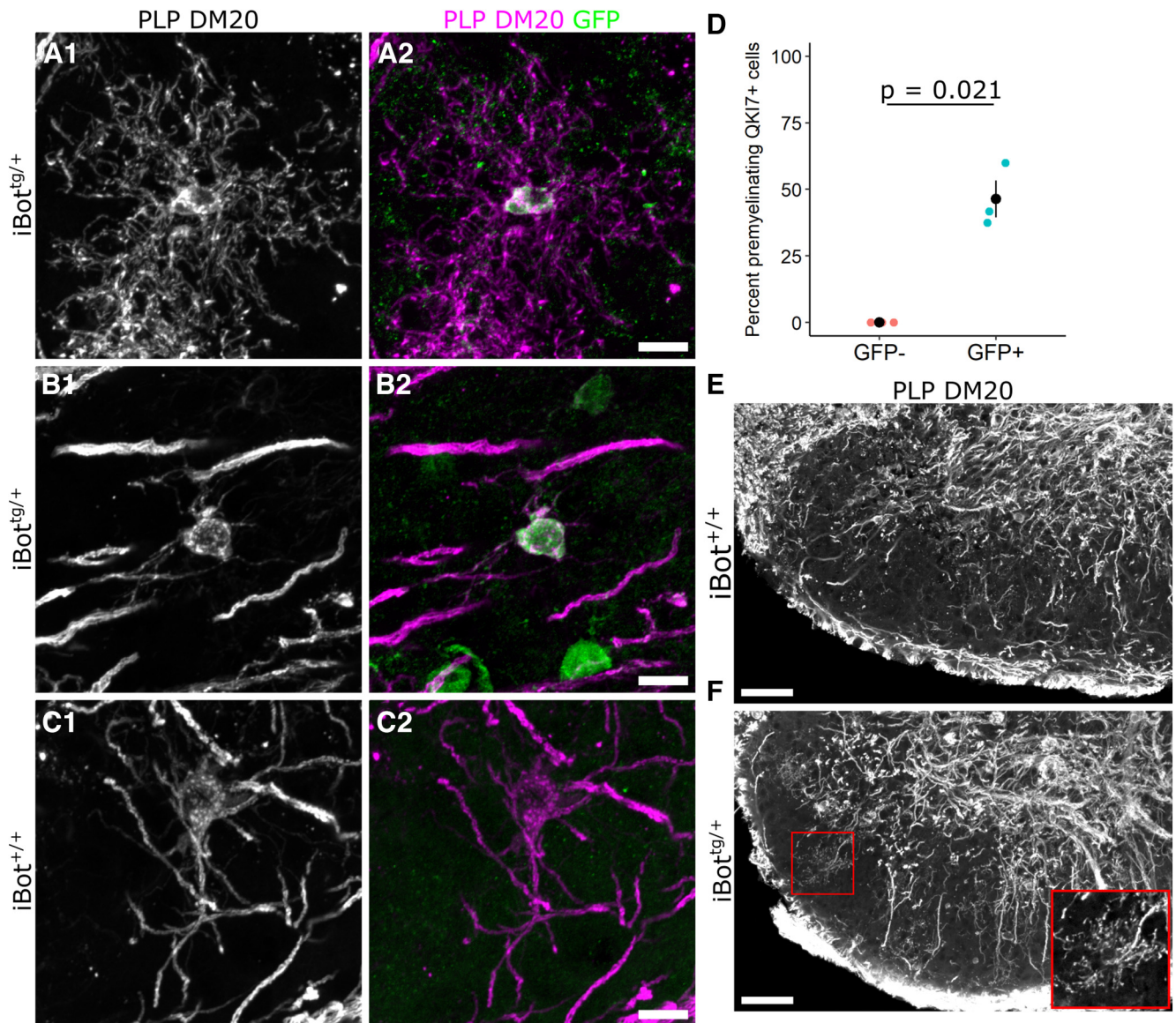


**Figure 7.** Morphologic features of *iBot*<sup>tg/+</sup> and *iBot*<sup>+/+</sup> OLs in the dorsal horn at P13. **A–C**, Double label for PLP/DM20 and GFP in *iBot*<sup>tg/+</sup> (**A, B**) and *iBot*<sup>+/+</sup> mice (**C**) showing a premyelinating OL (**A**) or myelinating OLs (**B, C**) in the dorsal horn at P13. **D**, Percentage of QKI7+ OLs scored as having a premyelinating morphology among GFP– OLs (0%) and GFP+ OLs ( $46.4 \pm 6.9\%$ , Welch’s two sample *t* test,  $t_{(2)} = -6.712$ ,  $p = 0.021$ ,  $n = 3$  *iBot*<sup>tg/+</sup> animals, cells were scored from two different images taken in the dorsal horn of each animal). **E, F**, Low-magnification images of PLP/DM20 labeling in the dorsal horn of *iBot*<sup>+/+</sup> (**E**) and *iBot*<sup>tg/+</sup> (**F**) mice at P13. Inset shows a magnified view of the premyelinating OL from the region outlined in red (**F**).  $\gamma$  Was adjusted to 0.5 (**E, F**) to better visualize premyelinating OLs. Scale bars = 10  $\mu$ m (**A–C**), 50  $\mu$ m (**E, F**).

$10^3$  a.u.) compared with control cells ( $9.83 \times 10^3 \pm 757$  a.u.; Fig. 8D).

As it was difficult to assess the distribution of Fyn within the processes of individual QKI7-labeled OLs in the dorsal column, we also wanted to address the possibility that Fyn may accumulate in the somas of *iBot*<sup>tg/+</sup> OLs because of a VAMP2/3-dependent trafficking defect. To do this, we examined *iBot*<sup>tg/+</sup> OLs in the dorsal gray matter using PLP-DM20 labeling to better visualize the morphology of individual cells. Here, we saw strong Fyn staining not just in the soma and proximal processes, but throughout the more distal processes as well (Fig. 8E), indicating that its transport into the processes was not defective in the *iBot*<sup>tg/+</sup> OLs.

#### Fyn expression is concentrated in NKX2.2–/GFP+ OLs in *iBot*<sup>tg/+</sup> mice

To further investigate the differentiation status of the stalled *iBot*<sup>tg/+</sup> OLs and clarify the relationship between Fyn kinase

expression and the maturation defect observed, we performed double labeling for total Fyn and NKX2.2 in the dorsal gray matter of *iBot*<sup>+/+</sup> and *iBot*<sup>tg/+</sup> spinal cords. Compared with the dorsal gray matter of control mice, Fyn staining in *iBot*<sup>tg/+</sup> mice appeared concentrated within relatively large, GFP+/NKX2.2– cells (Fig. 9A,B). Their lack of NKX2.2 expression indicated that they were not actively differentiating OLs, but that they had also not reached the fully mature NKX2.2 re-expressing stage. A similar distribution of Fyn could also be observed in the dorsal cst white matter tract of *iBot*<sup>tg/+</sup> spinal cords (Fig. 9C).

To determine whether the overall level of Fyn expression was enhanced in the spinal cords of *iBot*<sup>tg/+</sup> mice, we performed Western blotting for Fyn using spinal cord lysates from *iBot*<sup>+/+</sup> and *iBot*<sup>tg/+</sup> mice (Fig. 9D). Normalization to GAPDH indicated that, while not enhanced, overall levels of Fyn in the *iBot*<sup>tg/+</sup> mice were very similar to controls (Fig. 9E), despite the significant reduction in overall OL density. This can likely be

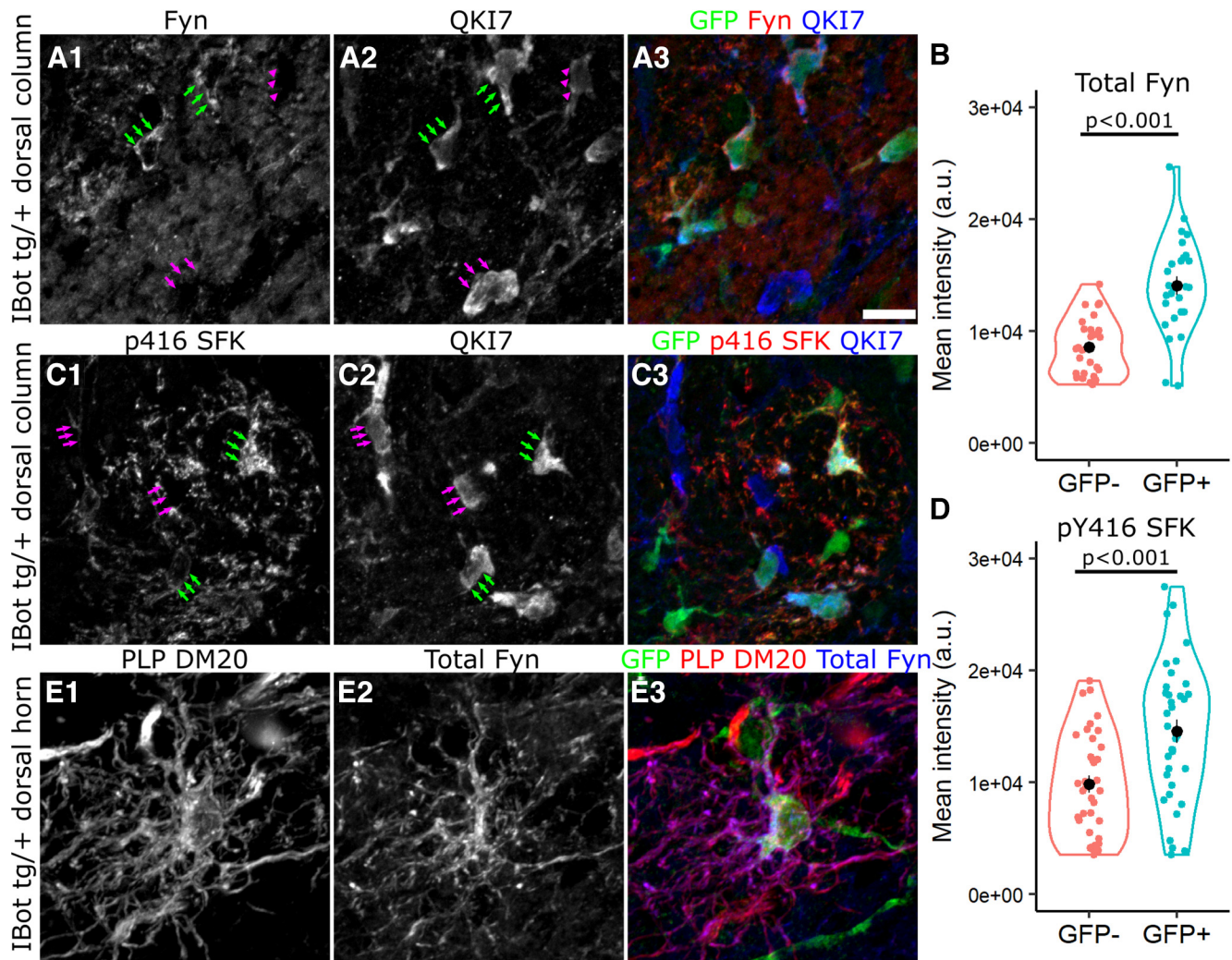


**Figure 8.** Fyn is highly expressed throughout the soma and processes of *iBot*<sup>tg/+</sup> OLs. **A, C,** Labeling for QKI7, GFP and either Fyn (**A**) or p416 SFK (**C**) around the border of *iBot*<sup>tg/+</sup> (GFP+, green arrows) and *iBot*<sup>+/+</sup> OLs (GFP–, magenta arrows) in *iBot*<sup>tg/+</sup> corticospinal tract. **B,** Average fluorescence intensity of Fyn staining along the edge of GFP– ( $8.61 \times 10^3 \pm 495.1$  a.u.) and GFP+ ( $1.41 \times 10^4 \pm 819.3$  a.u.) OLs in the dorsal column of *iBot*<sup>tg/+</sup> animals (Welch's two sample *t* test,  $t_{(42.76)} = -5.70$ ,  $p = 1.03 \times 10^{-6}$ ,  $n = 27$  cells per condition from 3 *iBot*<sup>tg/+</sup> animals). **D,** Average fluorescence intensity of p416 SFK staining along the edge of GFP– ( $9.83 \times 10^3 \pm 757$  a.u.) and GFP+ OLs ( $1.45 \times 10^4 \pm 1.03 \times 10^3$  a.u., Welch's two sample *t* test,  $t_{(64.13)} = -3.679$ ,  $p = 4.81 \times 10^{-4}$ ,  $n = 36$  cells per condition from 4 *iBot*<sup>tg/+</sup> animals). **E,** GFP+ premyelinating OL labeled for PLP/DM20, Fyn, and GFP in P13 *iBot*<sup>tg/+</sup> dorsal horn. Scale bar = 10  $\mu$ m (**A, C**).

explained, at least in part, by the increased prevalence of *iBot*<sup>tg/+</sup> OLs in the premyelinating stage, when *Fyn* expression normally peaks. However, qualitatively, the level of Fyn staining associated with the *iBot*<sup>tg/+</sup> OLs often appeared higher even than that of NKX2.2+ premyelinating OLs seen in control mice (Fig. 9B, inset), suggesting that an overaccumulation of Fyn in the *iBot*<sup>tg/+</sup> OLs may also contribute to the overall levels of Fyn detected in the *iBot*<sup>tg/+</sup> spinal cord lysates.

## Discussion

Robust and timely production of new, myelinating OLs is essential for successful CNS myelination in development as well as efficient myelin remodeling in adulthood. Here, we have shown that impairment of a subset of SNARE dependent processes, through toxin-mediated cleavage of VAMP2/3, resulted in a markedly diminished capacity to produce myelinating OLs in the developing mouse spinal cord, resulting in hypomyelination and significant motor impairment. Our data indicate that

VAMP2/3 become critical to the development of OL lineage cells once they have exited cell cycle and begun to differentiate. Interestingly, the production of OPCs, as well as their capacity to self-renew and initiate differentiation, appeared largely unaffected by the cleavage of VAMP2/3. During differentiation, however, OLs with cleaved VAMP2/3 appeared to stall in the premyelinating stage, ultimately failing to reach maturity. In addition to OL lineage cells, NG2-cre also drives expression of BoNT/B-LC in vascular pericytes. Labeling for Laminin+ endothelial cells in the *iBot*<sup>tg/+</sup> mice, however, did not reveal any gross abnormalities in spinal cord vasculature that might otherwise account for the impaired maturation of OL lineage cells.

BoNT/B specifically cleaves VAMP1, VAMP2, and VAMP3, but not VAMP4, VAMP5, VAMP7, VAMP8, or other SNARE proteins (Yamamoto et al., 2012). Since OL lineage cells primarily express VAMP2–VAMP4 and VAMP7 (Feldmann et al., 2009; Zhang et al., 2014), the observed effects are likely to have been mediated by cleavage of VAMP2/VAMP3. Although Cre is activated in vascular mural cells in addition to OL lineage cells in NG2-cre mice (Zhu et al., 2008), it is unlikely that the phenotype

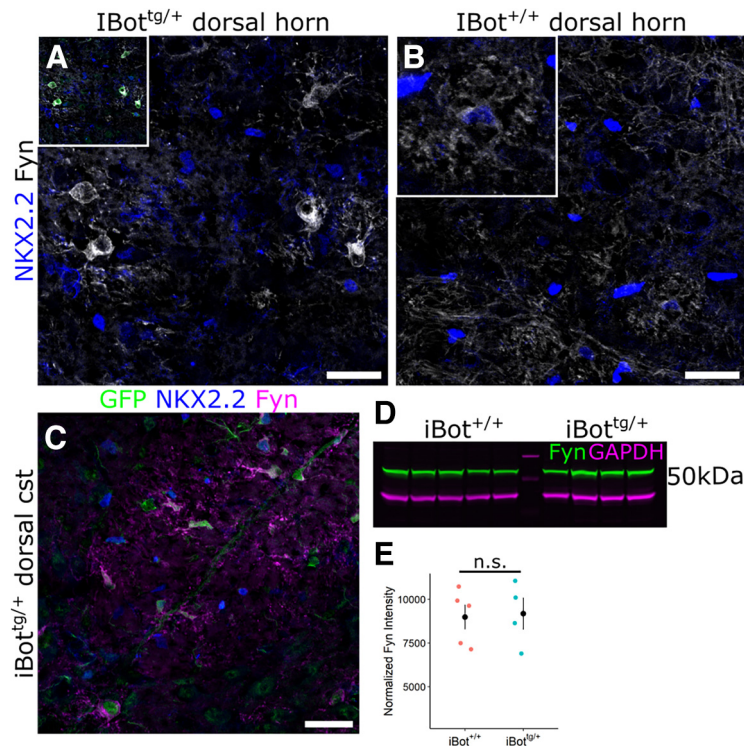


**Figure 9.** Fyn expression in *iBot*<sup>tg/+</sup> spinal cords is concentrated in NKX2.2—BoNT/B-expressing OLs. **A**, Immunolabeling for Fyn and NKX2.2 in *iBot*<sup>tg/+</sup> dorsal horn, inset shows overlay with GFP. **B**, Immunolabeling for Fyn and NKX2.2 *iBot*<sup>+/+</sup> dorsal horn, inset shows enlarged view of control premyelinating OL. **C**, GFP, NKX2.2, and Fyn labeling in *iBot*<sup>tg/+</sup> dorsal corticospinal tract. **D**, Western blot analysis for total Fyn (green) and GAPDH (magenta) from P14–P15 *iBot*<sup>+/+</sup> and *iBot*<sup>tg/+</sup> spinal cord lysates. **E**, Quantification of total Fyn signal normalized to GAPDH from *iBot*<sup>+/+</sup> ( $8.99 \times 10^3 \pm 705.49$  a.u.) and *iBot*<sup>tg/+</sup> ( $9.18 \times 10^3 \pm 907.86$  a.u.) spinal cord lysates (Welch's two sample *t* test,  $t_{(6,06)} = -0.168$ ,  $p = 0.872$ ,  $n = 5$  *iBot*<sup>+/+</sup> and 4 *iBot*<sup>tg/+</sup> mice). Scale bar = 25  $\mu$ m (**A–C**).

is because of off-target effects of by VAMP cleavage in non-OL lineage cells, as similar cell-autonomous myelination defects occur in other mouse lines that target BoNT/B-LC to OL lineage cells, such as *iBot*;Pdgfra-creER and *iBot*;Cnp-cre (Lam et al., 2022; Pan et al., 2023). In addition, a mouse protein BLAST search for the amino acid sequence flanking the BoNT-B cleavage site [GASQFE] (G. Schiavo et al., 2000; Binz et al., 2010) returned VAMP1, VAMP2, and VAMP3 as the only proteins exhibiting a complete match, further corroborating the interpretation that the effects observed in the *iBot*<sup>tg/+</sup> mice are likely to have been caused by cleavage of VAMP2/3 in OL lineage cells. Furthermore, knock-down of *Vamp2* in dissociated rat OL cultures impaired their maturation and elaboration of MBP+ myelin membranes. Knock-down of *Vamp3* also reduced the proportion of OLs with membranous process expansion by 50%, but the effect did not reach significance. Thus, the observed phenotype of overexpressing BoNT/B in OPCs is likely because of a cell autonomous effect of VAMP2/3 loss of function.

It is interesting that we did not observe any compensatory response among OPCs to the deficiency in OL number or myelination. For comparison, both jimpy and shiverer mice, two mutant mouse lines with a hypomyelination phenotype, show enhanced proliferation and density of OPCs as a result of insufficient myelination (Roach et al., 1983; Nave et al., 1987; Wu et al., 2000; Bu et al., 2004). One possibility is that loss of VAMP2/3 impairs the ability of OPCs to respond to abnormal environmental conditions such as hypomyelination. Alternatively, the prevalence of premyelinating OLs, despite not exceeding the total number of OLs in control animals, could discourage the response of OPCs

to hypomyelination through factors specifically expressed in the premyelinating stage. While these possibilities are speculative, they may be relevant in the context of demyelinating disease, where identification of factors that could desensitize OPCs to their environment may provide new targets for therapeutic strategies aimed at promoting remyelination.

Our data indicate that cleavage of VAMP2/3 in the OL lineage primarily impacts cells in the early OL stage of development and suggest that VAMP2/3-dependent processes play a major role in managing this crucial period of OL differentiation. EdU pulse chase labeling of proliferative cells in developing *iBot*<sup>tg/+</sup> and control mice indicated that the rate of new OL production was not significantly affected by loss of VAMP2/3, suggesting that VAMP2/3 function is not critical to the development of OL lineage cells before the onset of differentiation. This was further supported by the observation that the density of NKX2.2<sup>high</sup> actively differentiating OLs in the dorsal column was similar between *iBot*<sup>tg/+</sup> mice and controls. The reduced proportion of OLs labeled by the mature OL markers GST $\pi$  and ASPA in the *iBot*<sup>tg/+</sup> mice suggested that their diminished capacity to produce OLs may have been because of a defect in maturation of differentiating OLs. Immunolabeling for NKX2.2 in the dorsal column further indicated that the reduced NKX2.2+ OL density was specific to a lack of fully mature OLs, which re-express NKX2.2 at low levels. Together, this suggests that VAMP2/3 serves an essential function late in the OL differentiation program, possibly by mediating the secretion and/or trafficking of a hypothetical molecule X (Fig. 10) that is required for OLs to become fully mature. Mice in which expression of BoNT/B is regulated by the *Cnp* promoter are defective in elaborating myelin membranes (Lam et al., 2022). In addition, the increased prevalence of *iBot*

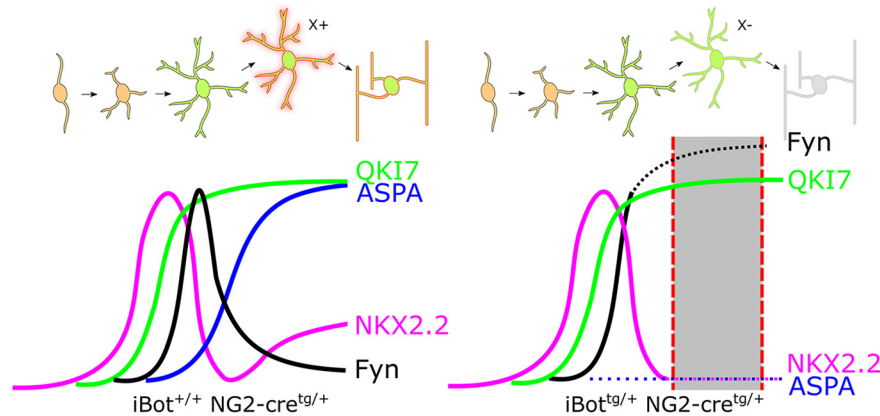


**Figure 10.** Proposed model of OL lineage development and gene expression timing in  $iBot^{+/+}$  and  $iBot^{tg/+}$  spinal cords. Dotted lines indicate abnormal expression timing observed in the  $iBot^{tg/+}$  mice relative to control, while the shaded region denotes the approximate stage in which  $iBot^{tg/+}$  OLs are lost. Impaired VAMP2/3-dependent secretion and/or trafficking of a hypothetical molecule X is indicated at the transition between premyelinating and myelinating stages of development.

expressing OLs with premyelinating morphology indicated that their progression through this stage may be extended, or that they may linger in the final stages of maturation, before being lost.

Given that the rate of new OL production did not appear affected in the  $iBot^{tg/+}$  mice, the reduced overall density of QKI7+ OLs and the strong reduction in the density of mature NKX2.2<sup>low</sup> re-expressing OLs implies that VAMP2/3-deficient OLs ultimately undergo cell death. Staining for cCasp3 indicated that, while not severe, the  $iBot^{tg/+}$  mice do exhibit increased cell death in the dorsal column, largely occurring within OL lineage cells labeled by Olig2. One possibility is that delayed development, or a prolonged premyelinating stage, may trigger apoptosis driven by an intrinsic cell death timer. It has been shown that the premyelinating stage of OL development is under strict temporal control (Czopka et al., 2013; Hill et al., 2014) and that a significant portion of newly generated OLs ultimately undergo apoptosis (Barres et al., 1992; Trapp et al., 1997; Hughes et al., 2018). Therefore, it is possible that a prolonged early OL stage in OLs with cleaved VAMP2/3 could trigger apoptosis by impairing timely axon-OL contact and initiation of myelination.

While our results suggest many of the  $iBot^{tg/+}$  OLs seem to be stalled in the premyelinating stage, some did appear to display morphology consistent with actively myelinating cells. This may indicate that VAMP2/3 function becomes critical just as premyelinating OLs begin to contact axons and initiate myelination. As a result,  $iBot^{tg/+}$  OLs observed with a more mature morphology may have been still in the initial stages of myelination, before undergoing cell death. Alternatively, there may be heterogeneity among OLs in their requirement for VAMP2/3 to complete differentiation successfully. This heterogeneity could either be innate and cell-specific or determined by the microenvironment around a given OL, including the type and number of axons contacted or available for contact. It is also possible, however, that those  $iBot^{tg/+}$  OLs which achieved a more mature developmental stage had been derived from escaped OPCs expressing EGFP but not BoNT/B-LC or cells in which the amount of BoNT/B-LC produced was insufficient to fully prevent their development.

Our data suggest that a VAMP2/3-dependent mechanism regulates the successful transition from the premyelinating to myelinating stage of OL development. It is possible that this mechanism involves the SNARE mediated trafficking and/or secretion of some molecule X that is required for differentiating OLs to progress beyond the premyelinating stage, and that

functional loss of this molecule X in the  $iBot^{tg/+}$  OLs is what leads to their stalled differentiation (Fig. 10). Another indication that the  $iBot^{tg/+}$  OLs undergo an extended premyelinating stage is their increased level of Fyn, which may have accumulated because of their stalling in a normally high Fyn-expressing stage. Our immunofluorescent localization of Fyn in  $iBot^{tg/+}$  premyelinating OLs showed that Fyn appeared to be highly expressed and present throughout both the soma and distal processes. This indicated that, in addition to being expressed and exhibiting markers of activation (SFK pY416+), Fyn was also being successfully trafficked out to sites of potential axon-OL contact, suggesting that the higher levels of Fyn and pY416 detected in the soma of OLs with cleaved VAMP2/3 (Fig. 8) was not because of accumulation caused by trafficking defects.

Western blotting for Fyn indicated that the overall level of Fyn expressed in  $iBot^{tg/+}$  spinal cords was similar to controls, despite a significantly reduced OL density in the  $iBot^{tg/+}$  spinal cords. As Fyn expression typically peaks in the premyelinating stage, the increased prevalence of premyelinating OLs in  $iBot^{tg/+}$  mice would be expected to offset the reduction in total Fyn levels to a degree. However, immunofluorescent labeling for Fyn further suggested that the  $iBot^{tg/+}$  OLs may exhibit even higher levels of Fyn than would be normally expected from peak Fyn expression during the premyelinating stage. In addition, we observed that the  $iBot^{tg/+}$  OLs displaying the strongest Fyn immunoreactivity were largely NKX2.2<sup>-</sup>, indicating they had completed the initial downregulation of NKX2.2 that occurs in the final stages of maturation. This provided further support for our interpretation that the increased level of Fyn seen in the  $iBot^{tg/+}$  OLs may have resulted, at least in part, from a prolonged accumulation of Fyn because of their stalled progression in the premyelinating stage, as summarized in Figure 10. Additionally, negative feedback on Fyn expression that might normally be exerted by mature OLs would be greatly reduced in the  $iBot^{tg/+}$  mice, which may further drive over-expression of Fyn. Alternatively, it is also possible that prolonged Fyn signaling itself could prevent differentiating OLs from reaching full maturity because of a failure to downregulate Fyn via a VAMP2/3-dependent mechanism. While it is unclear based on our data if VAMP2/3 is required for the downregulation of Fyn following differentiation, it is possible that the mechanism responsible is impaired by loss of VAMP2/3, ultimately leading to sustained Fyn expression and undermining OL lineage cell development.

Overall, our results show that VAMP2/3 play an essential role in regulating spinal cord OL differentiation during development. Differentiating OLs lacking functional VAMP2/3 appeared to undergo an extended, and ultimately unsuccessful, premyelinating stage, exhibiting expression profiles that indicated they were neither actively differentiating nor fully mature. Conversely, OPCs appeared relatively insensitive to VAMP2/3 cleavage and maintained their capacity for self-renewal as well as their ability to initiate differentiation. Taken together, our data suggest that a VAMP2/3-dependent mechanism active late in the differentiation process, during the transient downregulation of NKX2.2, is required for successful maturation of differentiating OLs to occur. While the precise nature of this mechanism is unclear, it may involve the trafficking, secretion, or membrane presentation of key axon-OL signaling factors via a VAMP2/3-specific pathway.

## References

- Barres BA, Hart IK, Coles HSR, Burne JF, Voyvodic JT, Richardson WD, Raff MC (1992) Cell death and control of cell survival in the oligodendrocyte lineage. *Cell* 70:31–46.
- Bijlard M, Klunder B, de Jonge JC, Nomden A, Tyagi S, de Vries H, Hoekstra D, Baron W (2015) Transcriptional expression of myelin basic protein in oligodendrocytes depends on functional syntaxin 4: a potential correlation with autocrine signaling. *Mol Cell Biol* 35:675–687.
- Bin JM, Harris SN, Kennedy TE (2016) The oligodendrocyte-specific antibody ‘CCI’ binds quaking 7. *J Neurochem* 139:181–186.
- Binz T, Sikorra S, Mahrhold S (2010) Clostridial neurotoxins: mechanism of SNARE cleavage and outlook on potential substrate specificity reengineering. *Toxins (Basel)* 2:665–682.
- Bu J, Banki A, Wu Q, Nishiyama A (2004) Increased NG2+ glial cell proliferation and oligodendrocyte generation in the hypomyelinating mutant shiverer. *Glia* 48:51–63.
- Butt AM, Ibrahim M, Berry M (1997) The relationship between developing oligodendrocyte units and maturing axons during myelinogenesis in the anterior medullary velum of neonatal rats. *J Neurocytol* 26:327–338.
- Cai J, Zhu Q, Zheng K, Li H, Qi Y, Cao Q, Qiu M (2010) Co-localization of Nkx6.2 and Nkx2.2 homeodomain proteins in differentiated myelinating oligodendrocytes. *Glia* 58:458–468.
- Chen S, Hall C, Barbieri JT (2008) Substrate recognition of VAMP-2 by botulinum neurotoxin B and tetanus neurotoxin. *J Biol Chem* 283:21153–21159.
- Colognato H, Ramachandrapa S, Olsen IM, ffrench-Constant C (2004) Integrins direct Src family kinases to regulate distinct phases of oligodendrocyte development. *J Cell Biol* 167:365–375.
- Czopka T, ffrench-Constant C, Lyons DA (2013) Individual oligodendrocytes have only a few hours in which to generate new myelin sheaths in vivo. *Dev Cell* 25:599–609.
- Dugas JC, Emery B (2013) Purification of oligodendrocyte precursor cells from rat cortices by immunopanning. *Cold Spring Harb Protoc* 2013:745–758.
- Fekete CD, Nishiyama A (2022) Presentation and integration of multiple signals that modulate oligodendrocyte lineage progression and myelination. *Front Cell Neurosci* 16:1041853.
- Feldmann A, Winterstein C, White R, Trotter J, Krämer-Albers EM (2009) Comprehensive analysis of expression, subcellular localization, and cognate pairing of SNARE proteins in oligodendrocytes. *J Neurosci Res* 87:1760–1772.
- Feldmann A, Amphornrat J, Schönherr M, Winterstein C, Möbius W, Ruhwedel T, Danglot L, Nave KA, Galli T, Bruns D, Trotter J, Krämer-Albers EM (2011) Transport of the major myelin proteolipid protein is directed by VAMP3 and VAMP7. *J Neurosci* 31:5659–5672.
- Floriddia EM, Lourenço T, Zhang S, van Bruggen D, Hilscher MM, Kukanja P, Gonçalves dos Santos JP, Altunkök M, Yokota C, Llorens-Bobadilla E, Mulinyawe SB, Grãos M, Sun LO, Frisén J, Nilsson M, Castelo-Branco G (2020) Distinct oligodendrocyte populations have spatial preference and different responses to spinal cord injury. *Nat Commun* 11:5860.
- Hill RA, Patel KD, Goncalves CM, Grutzendler J, Nishiyama A (2014) Modulation of oligodendrocyte generation during a critical temporal window after NG2 cell division. *Nat Neurosci* 17:1518–1527.
- Hughes EG, Orthmann-Murphy JL, Langseth AJ, Bergles DE (2018) Myelin remodeling through experience-dependent oligodendrogenesis in the adult somatosensory cortex. *Nat Neurosci* 21:696–706.
- Humeau Y, Doussau F, Grant NJ, Poulain B (2000) How botulinum and tetanus neurotoxins block neurotransmitter release. *Biochimie* 82:427–446.
- Kessaris N, Fogarty M, Iannarelli P, Grist M, Wegner M, Richardson WD (2006) Competing waves of oligodendrocytes in the forebrain and postnatal elimination of an embryonic lineage. *Nat Neurosci* 9:173–179.
- Lam M, Takeo K, Almeida RG, Cooper MH, Wu K, Iyer M, Kantarci H, Zuchero JB (2022) CNS myelination requires VAMP2/3-mediated membrane expansion in oligodendrocytes. *Nat Commun* 13:5583.
- Laursen LS, Chan CW, ffrench-Constant C (2009) An integrin-contactin complex regulates CNS myelination by differential Fyn phosphorylation. *J Neurosci* 29:9174–9185.
- Marques S, et al. (2016) Oligodendrocyte heterogeneity in the mouse juvenile and adult central nervous system. *Science* 352:1326–1329.
- Matrone C, Petrillo F, Nasso R, Ferretti G (2020) Fyn tyrosine kinase as harmonizing factor in neuronal functions and dysfunctions. *Int J Mol Sci* 21:4444.
- Medved J, Wood WM, Van Heyst MD, Sherafat A, Song JY, Sakya S, Wright DL, Nishiyama A (2021) Novel guanidine compounds inhibit platelet-derived growth factor receptor alpha transcription and oligodendrocyte precursor cell proliferation. *Glia* 69:792–811.
- Mitew S, Hay CM, Peckham H, Xiao J, Koenning M, Emery B (2014) Mechanisms regulating the development of oligodendrocytes and central nervous system myelin. *Neuroscience* 276:29–47.
- Nave KA, Bloom FE, Milner RJ (1987) A single nucleotide difference in the gene for myelin proteolipid protein defines the jimpy mutation in mouse. *J Neurochem* 49:1873–1877.
- Nishiyama A, Suzuki R, Zuo H, Zhu X (2010) Oligodendrocyte progenitor cell culture. In: *Protocols for neural cell culture Springer Protocols Handbook* (Doering LC, ed), Ed 4, Chapter 12. Totowa: Humana Press.
- Nishiyama A, Boshans L, Goncalves CM, Wegrzyn J, Patel KD (2016) Lineage, fate, and fate potential of NG2-glia. *Brain Res* 1638:116–128.
- Pan S, Mayoral SR, Choi HS, Chan JR, Kheirbek MA (2020) Preservation of a remote fear memory requires new myelin formation. *Nat Neurosci* 23:487–499.
- Pan S, Trimarco A, Zhang AJ, Fujimori K, Urade Y, Sun LO, Taveggia C, Zhang Y (2023) Oligodendrocyte lineage cell exocytosis and L-type prostanoidin D synthase promote oligodendrocyte development and myelination. *Elife* 12:377441.
- Pfeiffer SE, Warrington AE, Bansal R (1993) The oligodendrocyte and its many cellular processes. *Trends Cell Biol* 3:191–197.
- Qi Y, Cai J, Wu Y, Wu R, Lee J, Fu H, Rao M, Sussel L, Rubenstein J, Qiu M (2001) Control of oligodendrocyte differentiation by the Nkx2.2 homeodomain transcription factor. *Development* 128:2723–2733.
- R Core Team (2021) R: a language and environment for statistical computing. Vienna: R Foundation for Statistical Computing. Available at: <https://www.R-project.org/>.
- Roach A, Boylan K, Horvath S, Prusiner SB, Hood LE (1983) Characterization of cloned cDNA representing rat myelin basic protein: absence of expression in brain of shiverer mutant mice. *Cell* 34:799–806.
- RStudio Team (2021) RStudio: integrated development environment for R. Boston: RStudio, PBC.
- Schiavo G, Matteoli M, Montecucco C (2000) Neurotoxins affecting neuroexocytosis. *Physiol Rev* 80:717–766.
- Schiavo GG, Benfenati F, Poulain B, Rossetto O, de Laurentis PP, DasGupta BR, Montecucco C (1992) Tetanus and botulinum-B neurotoxins block neurotransmitter release by proteolytic cleavage of synaptobrevin. *Nature* 359:832–835.
- Schindelin J, Arganda-Carreras I, Frise E, Kaynig V, Longair M, Pietzsch T, Preibisch S, Rueden C, Saalfeld S, Schmid B, Tinevez J-Y, White DJ, Hartenstein V, Eliceiri K, Tomancak P, Cardona A (2012) Fiji: an open-source platform for biological-image analysis. *Nat Methods* 9:676–682.
- Slezak M, et al. (2012) Relevance of exocytotic glutamate release from retinal glia. *Neuron* 74:504–516.
- Sun LO, Mulinyawe SB, Collins HY, Ibrahim A, Li Q, Simon DJ, Tessier-Lavigne M, Barres BA (2018) Spatiotemporal control of CNS myelination



- by oligodendrocyte programmed cell death through the TFEB-PUMA axis. *Cell* 175:1811–1826.e21.
- Tansey FA, Cammer W (1991) A Pi form of glutathione-S-transferase is a myelin-and oligodendrocyte-associated enzyme in mouse brain. *J Neurochem* 57:95–102.
- Trapp BD, Nishiyama A, Cheng D, Macklin W (1997) Differentiation and death of premyelinating oligodendrocytes in developing rodent brain. *J Cell Biol* 137:459–468.
- Tripathi RB, Jackiewicz M, McKenzie IA, Kougioumtzidou E, Grist M, Richardson WD (2017) Remarkable stability of myelinating oligodendrocytes in mice. *Cell Rep* 21:316–323.
- Umemori H, Sato S, Yagi T, Aizawa S, Yamamoto T (1994) Initial events of myelination involve Fyn tyrosine kinase signalling. *Nature* 367:572–576.
- Watanabe M, Hadzic T, Nishiyama A (2004) Transient upregulation of Nkx2.2 expression in oligodendrocyte lineage cells during remyelination. *Glia* 46:311–322.
- White R, Gonsior C, Krämer-Albers E-M, Stöhr N, Hüttelmaier S, Trotter J (2008) Activation of oligodendroglial Fyn kinase enhances translation of mRNAs transported in hnRNP A2-dependent RNA granules. *J Cell Biol* 181:579–586.
- White R, Krämer-Albers EM (2014) Axon-glia interaction and membrane traffic in myelin formation. *Front Cell Neurosci* 7:284.
- Wickham H, et al. (2019) Welcome to the tidyverse. *J Open Source Softw* 4:1686.
- Wu Q, Miller RH, Ransohoff RM, Robinson S, Bu J, Nishiyama A (2000) Elevated levels of the chemokine GRO-1 correlate with elevated oligodendrocyte progenitor proliferation in the jimpy mutant. *J Neurosci* 20:2609–2617.
- Yamamoto H, Ida T, Tsutsuki H, Mori M, Matsumoto T, Kohda T, Mukamoto M, Goshima N, Kozaki S, Ihara H (2012) Specificity of botulinum protease for human VAMP family proteins. *Microbiol Immunol* 56:245–253.
- Yamamura T, Konola JT, Wekerle H, Lees MB (1991) Monoclonal antibodies against myelin proteolipid protein: identification and characterization of two major determinants. *J Neurochem* 57:1671–1680.
- Yeung MSY, Zdunek S, Bergmann O, Bernard S, Salehpour M, Alkass K, Perl S, Tisdale J, Possnert G, Brundin L, Druid H, Frisén J (2014) Dynamics of oligodendrocyte generation and myelination in the human brain. *Cell* 159:766–774.
- Young KM, Psachoulia K, Tripathi RB, Dunn S-J, Cossell L, Attwell D, Tohyama K, Richardson WD (2013) Oligodendrocyte dynamics in the healthy adult CNS: evidence for myelin remodeling. *Neuron* 77:873–885.
- Zhang Y, Chen K, Sloan SA, Bennett ML, Scholze AR, O'Keefe S, Phatnani HP, Guarnieri P, Caneda C, Ruderisch N, Deng S, Liddelow SA, Zhang C, Daneman R, Maniatis T, Barres BA, Wu JQ (2014) An RNA-sequencing transcriptome and splicing database of glia, neurons, and vascular cells of the cerebral cortex. *J Neurosci* 34:11929–11947.
- Zhu X, Hill RA, Nishiyama A (2008) NG2 cells generate oligodendrocytes and gray matter astrocytes in the spinal cord. *Neuron Glia Biol* 4:19–26.
- Zhu X, Hill RA, Dietrich D, Komitova M, Suzuki R, Nishiyama A (2011) Age-dependent fate and lineage restriction of single NG2 cells. *Development* 138:745–753.
- Zuchero JB, Fu MM, Sloan SA, Ibrahim A, Olson A, Zaremba A, Dugas JC, Wienbar S, Caprioglio AV, Kantor C, Leonoudakis D, Lariosa-Willingham K, Kronenberg G, Gertz K, Soderling SH, Miller RH, Barres BA (2015) CNS myelin wrapping is driven by actin disassembly. *Dev Cell* 34:152–167.